

# CryoEM structures of membrane pore and prepore complex reveal cytolytic mechanism of Pneumolysin

Katharina van Pee, Alexander Neuhaus, Edoardo D'Imprima, Deryck J Mills, Werner Kühlbrandt\*, Özkan Yildiz\*

Department of Structural Biology, Max Planck Institute of Biophysics, Frankfurt am Main, Germany

**Abstract** Many pathogenic bacteria produce pore-forming toxins to attack and kill human cells. We have determined the 4.5 Å structure of the ~2.2 MDa pore complex of pneumolysin, the main virulence factor of *Streptococcus pneumoniae*, by cryoEM. The pneumolysin pore is a 400 Å ring of 42 membrane-inserted monomers. Domain 3 of the soluble toxin refolds into two ~85 Å β-hairpins that traverse the lipid bilayer and assemble into a 168-strand β-barrel. The pore complex is stabilized by salt bridges between β-hairpins of adjacent subunits and an internal α-barrel. The apolar outer barrel surface with large sidechains is immersed in the lipid bilayer, while the inner barrel surface is highly charged. Comparison of the cryoEM pore complex to the prepore structure obtained by electron cryo-tomography and the x-ray structure of the soluble form reveals the detailed mechanisms by which the toxin monomers insert into the lipid bilayer to perforate the target membrane.

DOI: [10.7554/eLife.23644.001](https://doi.org/10.7554/eLife.23644.001)

\*For correspondence: werner.kuehlbrandt@biophys.mpg.de (WK); Oezkan.Yildiz@biophys.mpg.de (ÖY)

Competing interest: See [page 18](#)

Funding: See [page 18](#)

Received: 28 November 2016

Accepted: 17 March 2017

Published: 21 March 2017

Reviewing editor: Sjors HW Scheres, MRC Laboratory of Molecular Biology, United Kingdom

© Copyright van Pee et al. This article is distributed under the terms of the [Creative Commons Attribution License](#), which permits unrestricted use and redistribution provided that the original author and source are credited.

## Introduction

Gram-positive bacteria, including the common wound-infecting *Staphylococcus aureus*, the virulent food-borne pathogen *Listeria monocytogenes*, and *Streptococcus pneumoniae* that causes pneumonia, utilize cholesterol-dependent cytolysins (CDCs) to attack and kill mammalian and human cells (Gilbert, 2005; Tweten, 2005). The bacteria produce and release CDCs as water-soluble monomers that attach to cholesterol-containing cell membranes, where they assemble into large, 200–500 Å cytolytic pores (Olofsson et al., 1993). X-ray structures of pneumolysin (PLY) from *S. pneumoniae* (Lawrence et al., 2015; Marshall et al., 2015; van Pee et al., 2016) show that the soluble toxin monomers are roughly rod-shaped and consist of four domains (D1–D4). Sequence comparison suggests that all CDCs have the same domain structure and therefore insert into target membranes in essentially the same way (Tweten et al., 2001). Although numerous biochemical studies have addressed the arrangement of monomers in the CDC prepore or pore complex (Hotze and Tweten, 2012; Tilley et al., 2005) and how they might penetrate the lipid bilayer (Shatursky et al., 1999), the detailed structure of the pore complex, and hence the exact mechanism of membrane insertion is unknown. The size heterogeneity of CDC prepores and pores has so far precluded structure determination at high resolution. We determined the structure of the ring-shaped ~2.2 MDa PLY pore complex by cryoEM. Together with our 2.4 Å x-ray structure of soluble PLY (van Pee et al., 2016) and a map of the prepore complex obtained by electron cryo-tomography, we can now describe the entire process of membrane attachment, prepore and pore formation in near-atomic detail. Given the high degree of sequence conservation amongst CDCs, it is likely that the same mechanism of membrane insertion holds for related bacterial toxins.

## Results

### CryoEM structure of the PLY pore complex

Ring-shaped pore complexes of wildtype PLY (PLY<sub>WT</sub>) forming on unilamellar, cholesterol-containing liposomes were solubilized with detergent. The size and homogeneity of solubilized PLY pores is detergent-dependent, as indicated by negative-stain and cryoEM (**Figure 1—figure supplement 1**). Pore diameters varied from 310 to 500 Å in DDM or 350 to 400 Å in Cymal-6. Replacing the detergent Cymal-6 by amphipol A8-35 (**Althoff et al., 2011; Lu et al., 2014**) resulted in a stable population that was sufficiently homogenous for single-particle cryoEM. 2D class averages indicated a roughly even distribution of views (**Figure 1—figure supplement 2A**). Pore complexes were rings of 42 subunits with an aggregate molecular mass of 2.2 MDa. In total, 6461 ring images were combined to generate a 3D map with 42-fold symmetry at 4.5 Å resolution (**Figure 1; Figure 1—figure supplements 2B and 3**). The final map of the pore complex has an outer diameter of 400 Å and a total height of 110 Å, of which ~80 Å protrudes from the membrane surface (**Figure 1**).

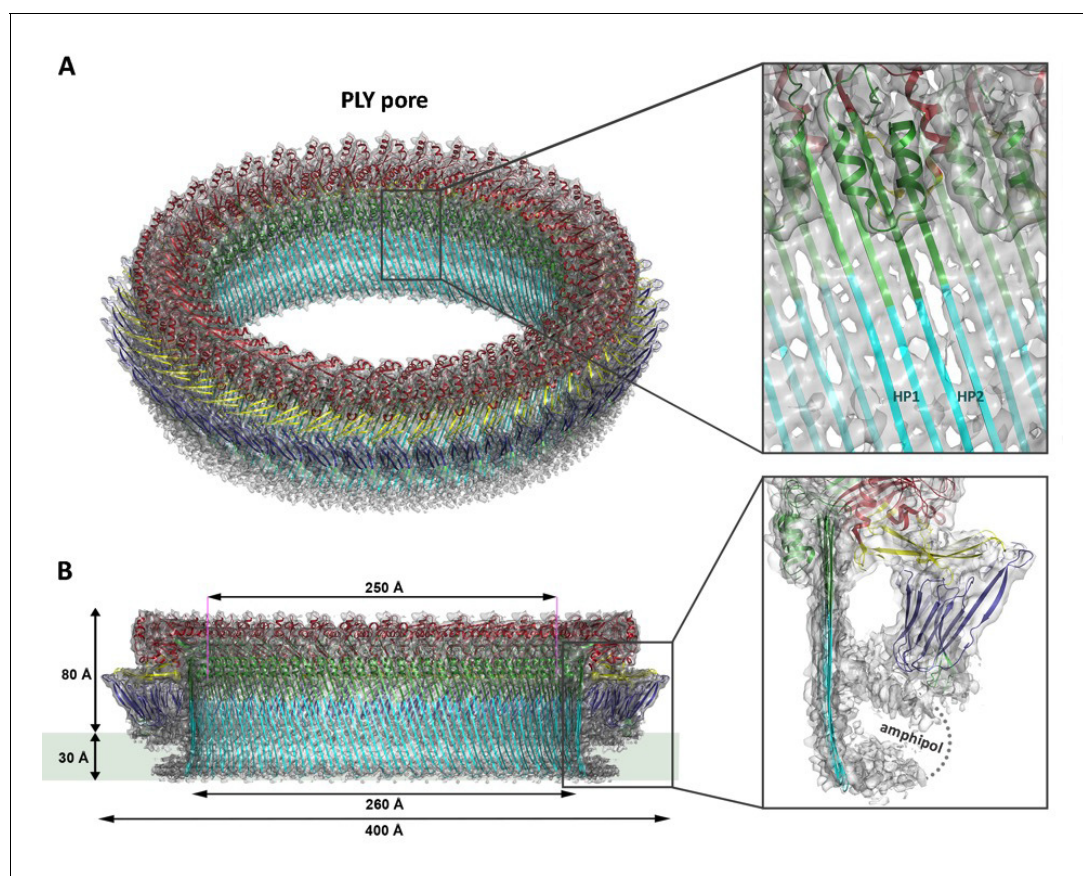


**Figure 1.** Overall structure of the PLY pore complex. (A) Single-particle cryoEM map of PLY at 4.5 Å resolution with fitted model. The four PLY domains (D1–D4) are red (D1), yellow (D2), green/cyan (D3) and blue (D4). Inset: refolded  $\beta$ -hairpins (HP1 and HP2) fitted to the map. Cyan  $\beta$ -strands have refolded from helix bundles in D3 of the soluble form. (B) Cross-section with overall dimensions of the pore complex. The grey bar indicates the position of the lipid bilayer. Inset: side view of membrane-inserted monomer with toroid density of disordered amphipol (broken line).

DOI: [10.7554/eLife.23644.002](https://doi.org/10.7554/eLife.23644.002)

The following figure supplements are available for figure 1:

**Figure supplement 1.** Negative stain and cryoEM of PLY solubilized in DDM, Cymal-6 and Amphipol.

DOI: [10.7554/eLife.23644.003](https://doi.org/10.7554/eLife.23644.003)

**Figure supplement 2.** Image processing of PLY rings.

DOI: [10.7554/eLife.23644.004](https://doi.org/10.7554/eLife.23644.004)

**Figure supplement 3.** Local resolution estimate of the PLY monomers and of the complete pore complex.

DOI: [10.7554/eLife.23644.005](https://doi.org/10.7554/eLife.23644.005)

Where possible, individual domains of the PLY x-ray structure (*van Pee et al., 2016*) were moved manually into the 4.5 Å cryoEM map as rigid bodies. Rebuilding of domains that refolded upon membrane insertion and readjustment of secondary structure elements and sidechains within domains yielded an atomic model of the pore complex (**Figure 1**). Comparison to the soluble form (**Figure 2A,B**) revealed a complete reorganization of the toxin upon membrane insertion. Of the four protein domains D1–D4 in the x-ray structure, D1 and D4 fitted the map of the pore complex with minimal modifications (**Figure 2—figure supplements 1–3, Video 1**). In the membrane-inserted form, the loop linking D1 to D2 refolds into a helix ( $\alpha$ 3a) at the interface between the rearranged domains D1, D2 and D3 (**Figures 2A,E, 3 and 4; Figure 2—figure supplement 4**). In D4, the highly conserved undecapeptide loop (**Figure 3**) that renders PLY cholesterol-specific (*Soltani et al., 2007b*) was shifted by up to  $\sim 9$  Å into the cryoEM map (**Figure 2—figure supplements 2 and 3, Video 1**). The undecapeptide loops of adjacent protomers in the pore complex are located in one plane on the outer membrane surface of the target cell, where they interact closely with the lipid head groups (**Figures 1B and 2A,C**). In the linear rows of soluble PLY monomers that are found in the PLY crystal structures (*Lawrence et al., 2015; Marshall et al., 2015; van Pee et al., 2016*), the distance between the loops of neighbouring monomers is  $\sim 14$  Å. In the pore complex this distance decreases to 4–5 Å, which enables an interaction of the loop that connects  $\beta$ -strands 18 and 19 ( $\beta$ 18/19) in D4 with the  $\beta$ 22/23 loop in D4 of the next monomer along the ring (**Figure 2—figure supplements 2 and 3, Video 1**). The close proximity of loop  $\beta$ 18/19 that contains Asp403, Thr405, and His407 of one monomer to loop  $\beta$ 18/19 and the undecapeptide containing Trp433 of the adjacent monomer suggests a critical role of these D4 loops not only in receptor recognition, but also in oligomer formation.

Domains 2 and 3 undergo massive rearrangement and refolding (**Figure 2A,B**) in the membrane-inserted form. The elongated two-stranded  $\beta$ -sheet of D2 rotates from its vertical position in the x-ray structure by  $90^\circ$  around a short glycine linker to an orientation parallel to the membrane plane in the pore complex. D2 connects D1 to D4, and its rotation results in a roughly linear translation of D1 by 35 Å towards the membrane surface and by 30 Å towards the pore centre. Otherwise, D2 required only minor adjustments of secondary structure for an optimal fit to the cryoEM map (**Figures 1B and 2A, Figure 2—figure supplement 5**).

By contrast, the structure of D3 changes entirely upon membrane insertion. In the soluble toxin, the central, five-stranded  $\beta$ -sheet in D3 is flanked by two bundles of short  $\alpha$ -helices (**Figure 2B**). In the pore complex, both bundles refold into four 85 Å  $\beta$ -strands, which form two parallel  $\beta$ -hairpins that insert into and traverse the lipid bilayer (**Figure 2A**). The  $\beta$ -hairpins of neighbouring subunits coalesce into one extensive, 168-strand  $\beta$ -barrel with an inner diameter of 260 Å (**Figure 1B**). The new  $\beta$ -strands can be traced unambiguously, because they are straight, apparently rigid and continuous with four  $\beta$ -strands in the D3 x-ray structure that are preserved in the membrane form. The two new, long  $\beta$ -hairpins are inclined by  $20^\circ$  relative to the membrane normal, in good agreement with predictions for perfringolysin O on the basis of cysteine crosslinking experiments (*Sato et al., 2013*). The chain trace in the refolded domain is confirmed by the positions of bulky densities for large sidechains in the  $\beta$ -barrel (**Figure 2D; Figure 2—figure supplement 4**). While five of the six helices in bundles HB1 and HB2 refold into  $\beta$ -strands in the pore complex, one remains intact. Conversely, the loop and fifth  $\beta$ -strand in the central  $\beta$ -sheet of D3 refold into a helix (**Figure 2A,B**). Together, the two  $\alpha$ -helices form a helix-turn-helix (HTH) motif (**Figure 2—figure supplement 4**). In the ring, the HTH motifs of the 42 subunits line up in one plane on the exoplasmic side of the molecule and form an  $\alpha$ -barrel inside the  $\beta$ -barrel (**Figures 1B and 4**), restricting the pore diameter locally to 250 Å (**Figure 1B**).

The outside of the membrane-inserted part of the  $\beta$ -barrel is almost entirely hydrophobic (**Figure 5A,E**) and covered by the toroid density of disordered amphipol that replaces the membrane lipid (**Figure 1B**), as in the cryoEM structures of amphipol-solubilized membrane proteins (*Althoff et al., 2011; Liao et al., 2013*). The inside pore surface is highly polar, with three aspartates and two glutamates forming a 15 by 9 Å patch of negative charge, flanked above and below by positive charges (**Figure 5B,F,G**). Apart from the hydrogen bonds between the 168  $\beta$ -strands in the barrel and the interactions of helix  $\alpha$ 3a with D1 and  $\beta$ -hairpin one (**Figure 2E, Figure 2—figure supplement 4**), three other factors contribute to pore stability: (1) the surface and charge complementarity of the membrane-inserted monomers (**Figure 5C**); (2) the alternating positive and negative charges of helices  $\alpha$ 13a and  $\alpha$ 13b in the  $\alpha$ -barrel (**Figure 5D**); and (3) ionic interactions between

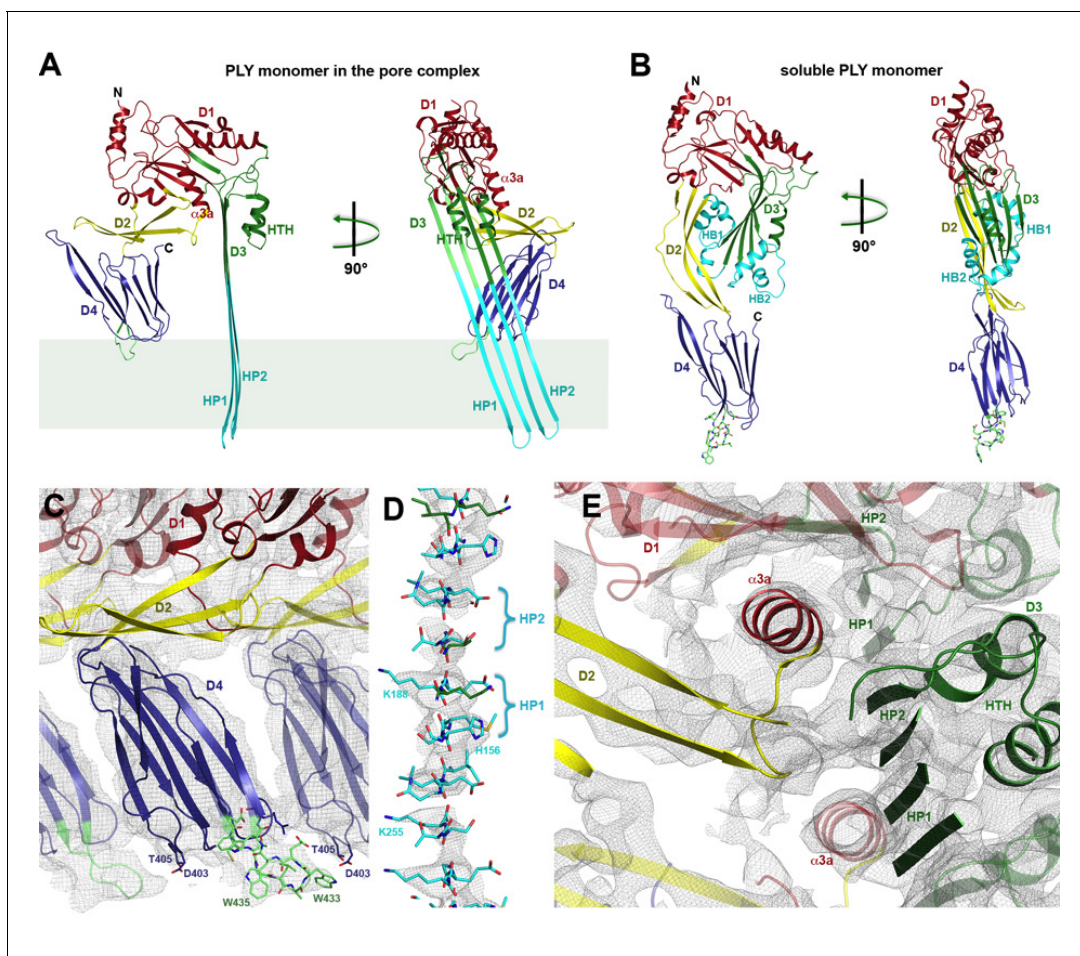


**Figure 2.** Soluble and membrane-inserted PLY monomer. One subunit of membrane-inserted form of PLY in the cryoEM structure (A) and x-ray structure of soluble PLY (*van Pee et al., 2016*) (B) seen from the side (left) and from the pore center (right). Both helix bundles (HB1 and HB2, cyan) in the PLY monomer refold to form two long, membrane-spanning  $\beta$ -hairpins (HP1 and HP2). The upper end of the  $\beta$ -hairpins is sandwiched between a helix-turn-helix motif (HTH, green) on the inside and helix  $\alpha$ 3a (red) of the next monomer on the outside of the pore. One of the helices is a refolded  $\beta$ -strand of D3 (green). Helix  $\alpha$ 3a is the refolded linker that connects D2 to D1 in the soluble monomer. (C) D4 contains the conserved undecapeptide (green sticks) that confers cholesterol specificity to PLY. The peptide includes three resolved Trp sidechains, one of which interacts with Thr405 in the adjacent monomer. (D) Cross section through a segment of the 168-strand  $\beta$ -barrel with resolved bulky sidechains. The two  $\beta$ -hairpins of one monomer are labelled. (E) Helix  $\alpha$ 3a interacts with HP1 and D1 of the neighbouring monomer, stabilizing the pore complex.

DOI: [10.7554/eLife.23644.006](https://doi.org/10.7554/eLife.23644.006)

The following figure supplements are available for figure 2:

**Figure supplement 1.** Stereo view of domain 1 presented as ribbon-and-stick model.

DOI: [10.7554/eLife.23644.007](https://doi.org/10.7554/eLife.23644.007)

**Figure supplement 2.** Superposition of domain 4 of the PLY monomer in the crystal structure (blue) and in the pore complex (green), viewed from the pore center.

DOI: [10.7554/eLife.23644.008](https://doi.org/10.7554/eLife.23644.008)

**Figure supplement 3.** Stereo view of domain 4 in the pore complex with potential inter- and intramolecular interactions of loops viewed from two sides.

DOI: [10.7554/eLife.23644.009](https://doi.org/10.7554/eLife.23644.009)

**Figure supplement 4.** Stereo view of domain 3 with the upper part of the  $\beta$ -barrel and the new helix-turn-helix motif (HTH) that forms the  $\alpha$ -barrel inside the pore.

DOI: [10.7554/eLife.23644.010](https://doi.org/10.7554/eLife.23644.010)

**Figure supplement 5.** Stereo view of domain 2 seen along the ring axis.

DOI: [10.7554/eLife.23644.011](https://doi.org/10.7554/eLife.23644.011)

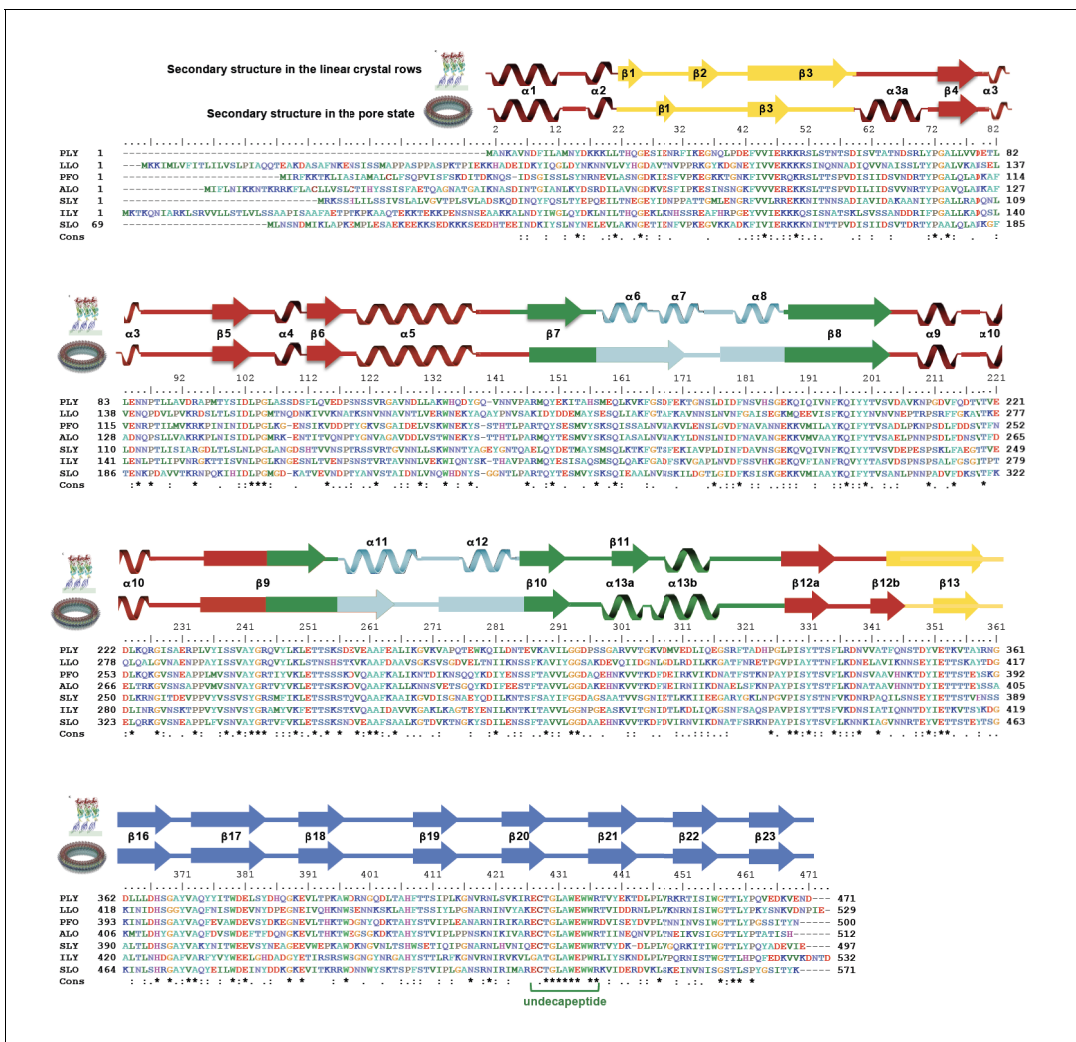


**Figure 3.** Sequence alignment of selected cholesterol-dependent cytolysins. Elements of secondary structure are shown for the crystal structure of soluble PLY (above) and for the cryoEM structure of the pore complex (below). Colors of the secondary structure elements and residue numbers correspond to the PLY crystal structure (**Figure 2B**; pdb code 5a0d). Asterisks indicate conserved residues.  
DOI: 10.7554/eLife.23644.012

charged sidechains in adjacent  $\beta$ -strands of the pore barrel (**Figure 5G**). In particular, Asp168 and Glu170 in  $\beta$ -strand  $\beta 7$  are in a good position for forming a salt bridge with Lys271 in  $\beta$ -strand  $\beta 10$  of the next-door monomer (**Figure 5G**).

### Three stages of PLY pore formation

To investigate the structures of the PLY prepore and pore complex in native membranes prior to detergent solubilisation, we incubated cholesterol-containing liposomes with purified PLY and generated 3D volumes by electron cryo-tomography (cryoET). The liposomes were studied with numerous ring-shaped complexes of 290 to 360 Å outer diameter (**Figure 6A**). Assemblies were identified as PLY pores or prepores by the absence or presence of a lipid bilayer within the ring (**Figure 7A**). Pore and prepore complexes were classified independently and processed by subtomogram averaging (**Figure 6B**). The subtomogram average map of the prepore complex at a resolution of 22 Å (**Figure 6C**) had an outer diameter of 320 Å and accommodated 34 subunits (**Figure 6D**). Of the available PLY crystal structures (Lawrence *et al.*, 2015; Marshall *et al.*, 2015; van Pee *et al.*, 2016), the model 5cr6 (Marshall *et al.*, 2015) fitted the map best (**Figure 6—figure supplement 1**), indicating that in this structure the soluble toxin is in the pre-pore state. The subtomogram average map of the pore complex at 27 Å resolution (**Figure 6C**) indicated a slightly larger diameter of

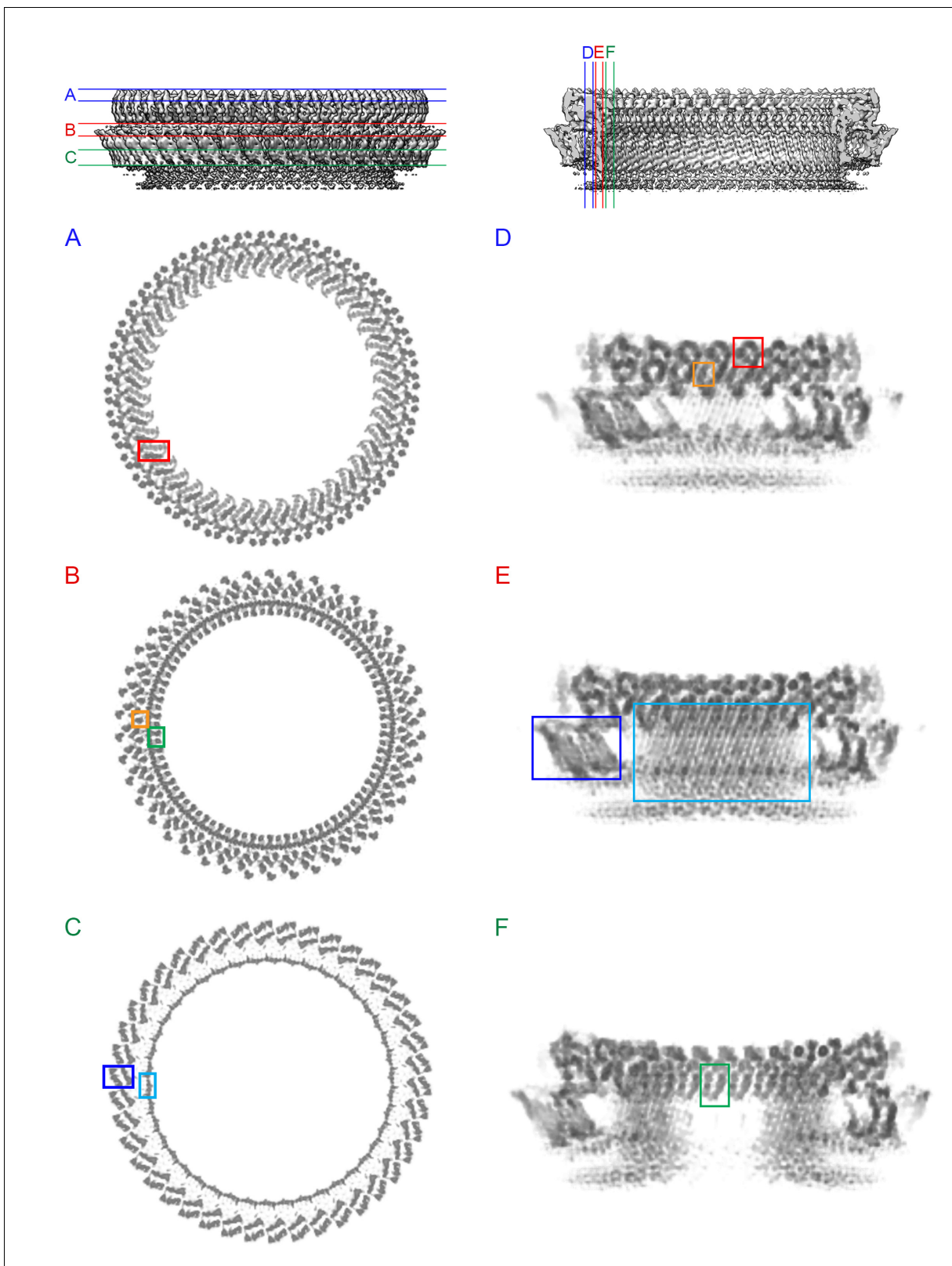


**Figure 4.** Intermolecular interactions in the 4.5 Å cryoEM map of the PLY pore complex. Slices parallel (A–C) and perpendicular (D–F) to the membrane reveal interactions of secondary structure elements between adjacent monomers in the pore complex. Section planes are indicated on top. Note that the scale of sections D to F is 50% larger to show molecular detail more clearly. The  $\beta 5$ - $\alpha 4$ - $\beta 6$  region in domain D1 and the long membrane-parallel helix  $\alpha 5$  (red box in A and D) alternate around the top of the pore complex. On the outside, the 168-strand  $\beta$ -barrel is flanked by helix  $\alpha 3a$  (orange box in A and D). *Figure 4 continued on next page*

Figure 4 continued

in **B** and **D**) and by the  $\alpha$ -barrel of the helix-turn-helix motifs (green box in **B** and **F**) on the inside. The 4-strand  $\beta$ -sheets of domain D4 (blue box in **C** and **E**) are offset against D4 of the next monomer, forming a ring of 8-strand  $\beta$ -sheets. The 85 Å-long  $\beta$ -strands forming the 168-strand  $\beta$ -barrel are clearly resolved (cyan box in **C** and **E**).

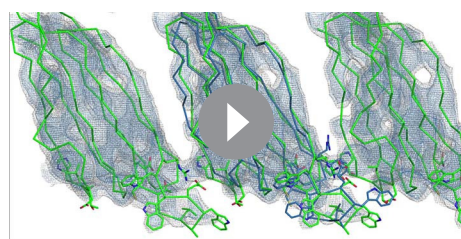
DOI: [10.7554/eLife.23644.013](https://doi.org/10.7554/eLife.23644.013)

around 350 Å, but likewise consisted of 34 subunits (**Figure 6E**). The cross-section profile resembled that of the high-resolution cryoEM map of the pore complex closely (**Figure 1**), indicating that solubilisation with detergent or amphipol does not change the structure of the membrane form significantly. The model of membrane-inserted PLY fitted the subtomogram average of the pore complex without significant adjustment, including the 20° inclination of the long  $\beta$ -hairpins relative to the membrane normal.

Atomic force microscopy (AFM) had revealed two different forms of PLY prepores in planar bilayers, rising 110 or 80 Å above the membrane surface (*van Pee et al., 2016*). The low form has the same height as the pore complex, but the lipid bilayer is still intact. We propose that in this lower prepore, D1, D2 and D4 have moved to their positions in the pore assembly, while D3 has not yet refolded and the long, membrane-spanning  $\beta$ -hairpins have not yet formed. We assign the tall form to an early prepore state, which then rearranges into the lower, late prepore state. The cross-section profile (**Figure 6B,D**) shows that the early prepore is essentially a ring-shaped side-by-side arrangement of soluble PLY monomers (**Figure 6—figure supplement 1**), similar to that in the crystal lattice (*Lawrence et al., 2015; Marshall et al., 2015; van Pee et al., 2016*). While the late prepore was observed for 13% of the rings on planar bilayers examined by AFM, it was not observed in tomographic volumes of PLY on liposomes, implying that it is an intermediate, transient state which inserts more readily into curved liposomes than into planar bilayers. Cross-sections of pore complexes in liposomes (**Figure 6B,E**) show that the lipid bilayer around the prepores and pores is curved, whereas in the AFM images it was flat (*van Pee et al., 2016*). Prepore stability and membrane insertion thus seem to be related to membrane curvature, such that pores form preferentially in lipid bilayers with a convex curvature.

## Determinants of lytic activity

To understand the functional role of individual sidechains in oligomerization, prepore and pore formation, we mutated Asp168 that, as the structure suggests, might be involved in forming a salt bridge between adjacent subunits to alanine (PLY<sub>D168A</sub>). We also deleted Ala146 and Arg147 (PLY<sub>Δ146/147</sub>) in the loop that would clash with the last  $\beta$ -strand of the central  $\beta$ -sheet. The resulting mutants were characterized by negative-stain EM (**Figure 7A**), hemolytic activity assays (**Figure 7B**), and x-ray crystallography (**Figure 8**). X-ray data were collected to 2.45 and 2.5 Å resolution from crystals of PLY<sub>D168A</sub> and PLY<sub>Δ146/147</sub> (**Table 1**). The structures were solved by molecular replacement with the x-ray structure of PLY<sub>WT</sub> (*van Pee et al., 2016*). As in PLY<sub>WT</sub>, the mutant monomers crystal-

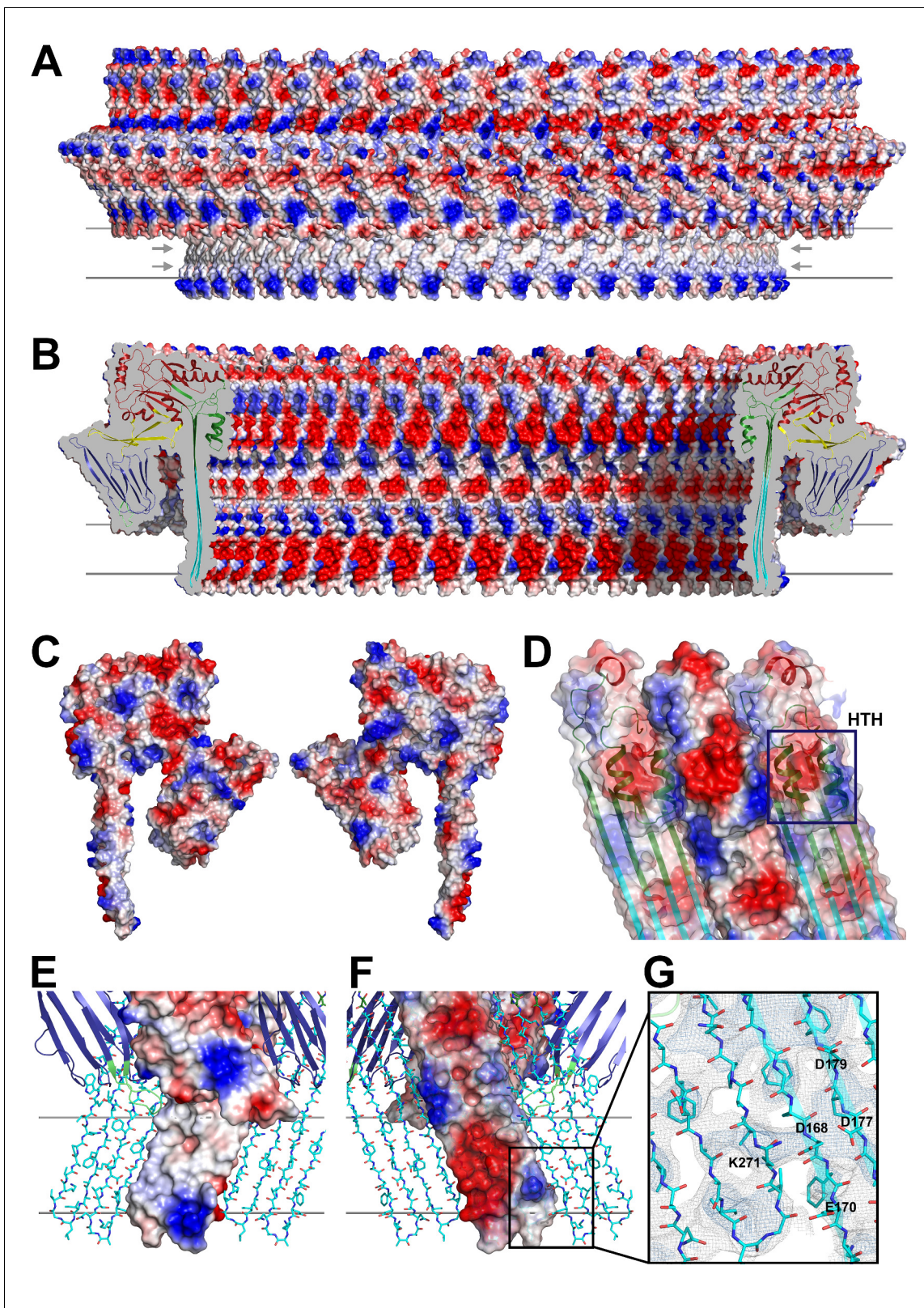


**Video 1.** Superposition of domain 4 of the PLY monomer from the crystal structure (blue) on domain 4 of the PLY monomer in the pore complex (green) rotated around an axis perpendicular to the membrane. Residues of the undecapeptide and selected residues in other loops are shown as sticks.

DOI: [10.7554/eLife.23644.014](https://doi.org/10.7554/eLife.23644.014)

lized in rows. Superposition of both structures on PLY<sub>WT</sub> showed no significant overall differences, although a detailed comparison indicated small changes in domain D2, helix bundle HB2 and in two of the D4 loops (**Figure 8**). Around the mutated residue in PLY<sub>D168A</sub> differences were restricted to sidechain orientations, while the deletion of two residues in PLY<sub>Δ146/147</sub> caused significant conformational changes in the loop connecting helix  $\alpha$ 5 to strand  $\beta$ 7 of the central  $\beta$ -sheet. This deletion also caused a slight shift of helix  $\alpha$ 5 towards D3 (**Figure 8**).

Even though the structures of PLY<sub>D168A</sub> and PLY<sub>Δ146/147</sub> were very similar to PLY<sub>WT</sub>, they displayed major differences in their membrane-binding and oligomerization behaviour. Like PLY<sub>WT</sub>, PLY<sub>D168A</sub> bound to cholesterol-containing



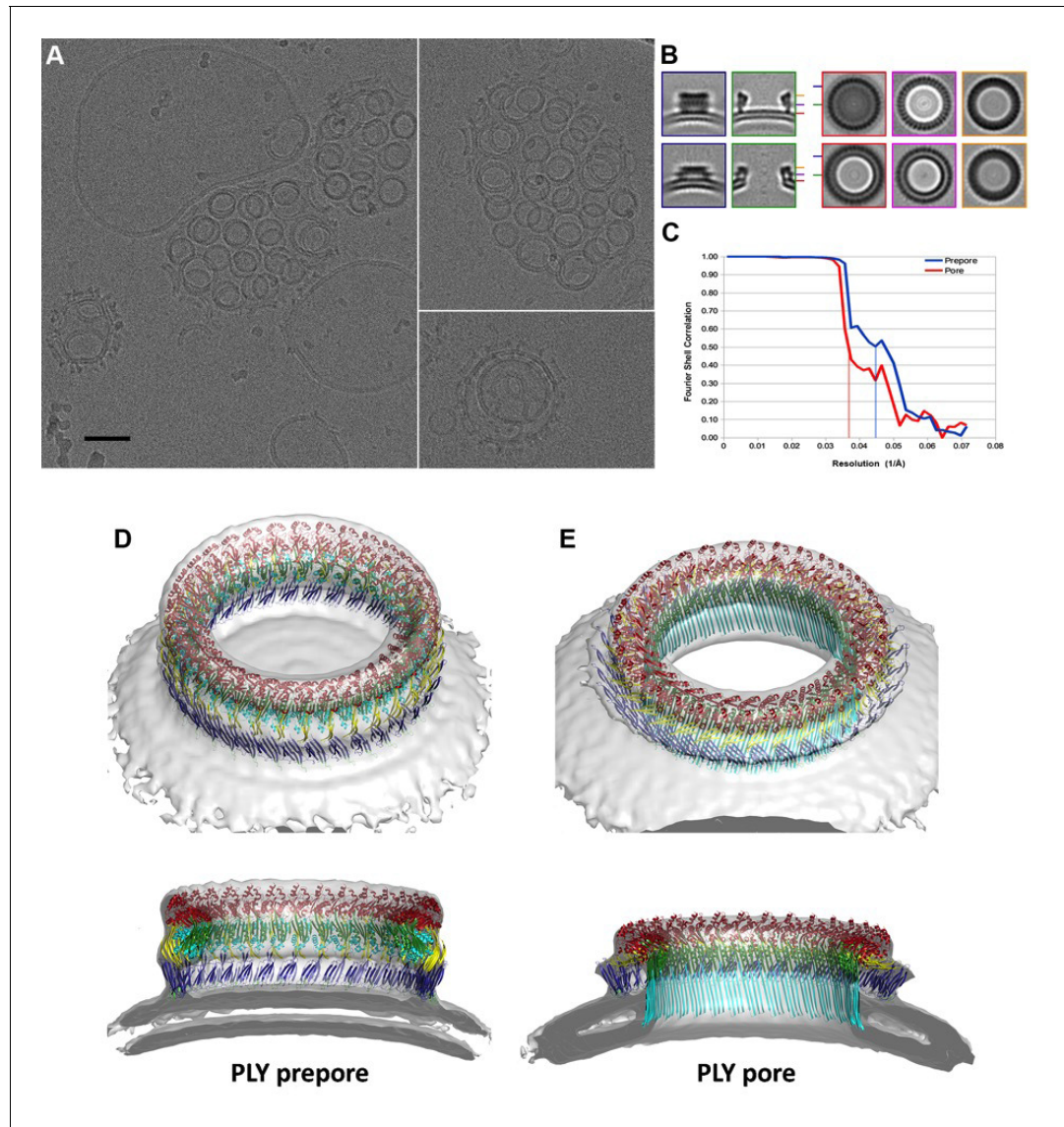
**Figure 5.** Charge distribution in the PLY pore complex. (A) Positive (blue) and negative charges (red) are evenly distributed on the polar outer surface of the pore complex. The membrane-inserted region is marked by a band of neutral hydrophobic residues (arrows). (B) The inner surface of the pore complex is highly charged. (C) Contact surfaces of adjacent PLY monomers in the pore complex. (D) Charge complementarity of the two helices in the helix-turn-helix motif forming the internal  $\alpha$ -barrel. Positive charges are shown in blue and negative charges in red. (E) The membrane-inserted region  
 Figure 5 continued on next page



Figure 5 continued

of the  $\beta$ -barrel is hydrophobic on the outside and negatively charged on the inside (F). The inset (G) shows map density for the salt bridge between Asp168 of one PLY monomer with Lys271 in the next monomer along the ring. Glutamates and aspartates forming the negatively charged patches on the inner surface of the  $\beta$ -barrel are drawn as sticks. The map is contoured at 5.0 and 6.0  $\sigma$ .

DOI: 10.7554/eLife.23644.015



**Figure 6.** CryoET of PLY prepores and pores. (A) PLY assembles into prepores and pores upon incubation with cholesterol-containing liposomes. Scale bar, 50 nm. (B) Sections through subtomogram average volumes of the prepore (top) and pore complex (below). Left panel: sections perpendicular to the membrane; right panel: sections parallel to the membrane. Colors indicate section planes. (C) Fourier shell correlation for subtomogram averages indicate 22 Å resolution for the prepore and 27 Å for the pore at FSC<sub>0.5</sub> or 20 Å and 21 Å resolution at FSC<sub>0.3</sub>. Oblique view (D) and cross section (E) of PLY prepore (left) and pore (right). Both maps accommodate 34 PLY monomers. The prepore map was fitted with the crystal structure of the soluble PLY monomer (Marshall *et al.*, 2015), and the pore map with the cryoEM structure of the pore monomer (Figure 2A). PLY domains are red (D1), yellow (D2), green/cyan (D3) and blue (D4). The lipid bilayer is continuous in the prepore complex, but absent in the pore complex. DOI: 10.7554/eLife.23644.016

The following figure supplement is available for figure 6:

**Figure supplement 1.** CryoET map of the PLY prepore with rigid-body fitted x-ray structures of the water-soluble toxin that forms rows in the 3D crystals.

DOI: 10.7554/eLife.23644.017

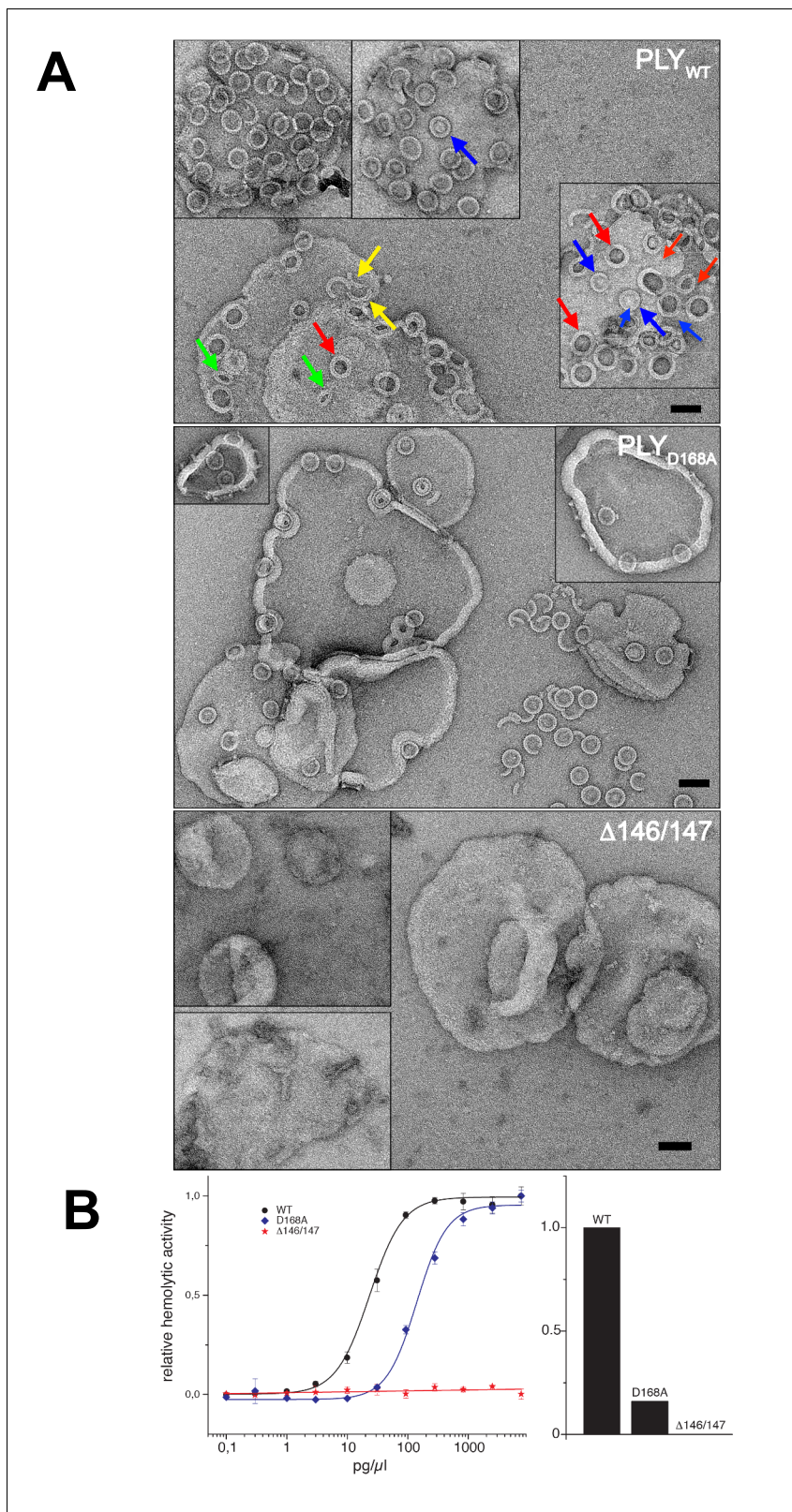


**Figure 7.** Membrane binding and hemolytic activity of PLY. (A) Wildtype PLY (PLY<sub>WT</sub>) and PLY<sub>D168A</sub> form rings on cholesterol-containing liposomes. PLY<sub>WT</sub> lyses the majority of liposomes, while PLY<sub>D168A</sub> leaves them mostly intact. Lipid-filled rings with a narrow rim (blue arrows) are prepores, while rings with a wider rim that do not contain lipid (red arrows) are pores. Slits (green arrows) and arcs (yellow arrows) are observed occasionally, but mostly PLY forms complete rings. Mutant PLY<sub>D168A</sub> prepores detach easily from the liposomes due to reduced binding affinity, and then break into fragments. Figure 7 continued on next page

Figure 7 continued

Curves indicate the hemolytic activity of PLY<sub>WT</sub>, PLY<sub>D168A</sub>, and PLY<sub>Δ146/147</sub>. PLY<sub>Δ146/147</sub> is inactive, in line with the inability of this mutant to form oligomers on cholesterol-containing liposomes. Scale bar: 50 nm.

DOI: 10.7554/eLife.23644.018

liposomes and oligomerized into rings (Figure 7A). However, unlike PLY<sub>WT</sub> that lysed the liposomes within a short time, liposomes incubated with PLY<sub>D168A</sub> remained intact for hours. Frequently, the rings detached from the liposomes, indicating they were prepores that had not yet inserted into the membrane. This is also reflected by the hemolytic activity, which was reduced by 80% compared to PLY<sub>WT</sub>, highlighting the important role of Asp168 in ionic interactions between  $\beta$ -strands that stabilize the pore complex.

PLY<sub>Δ146/147</sub> was not able to bind to the membranes at all and had no detectable hemolytic activity (Figure 7B). Ionic interactions between the  $\beta$ -strands thus contribute significantly to pore stability, and any disruption of these interactions compromises pore formation. Both mutations pinpoint

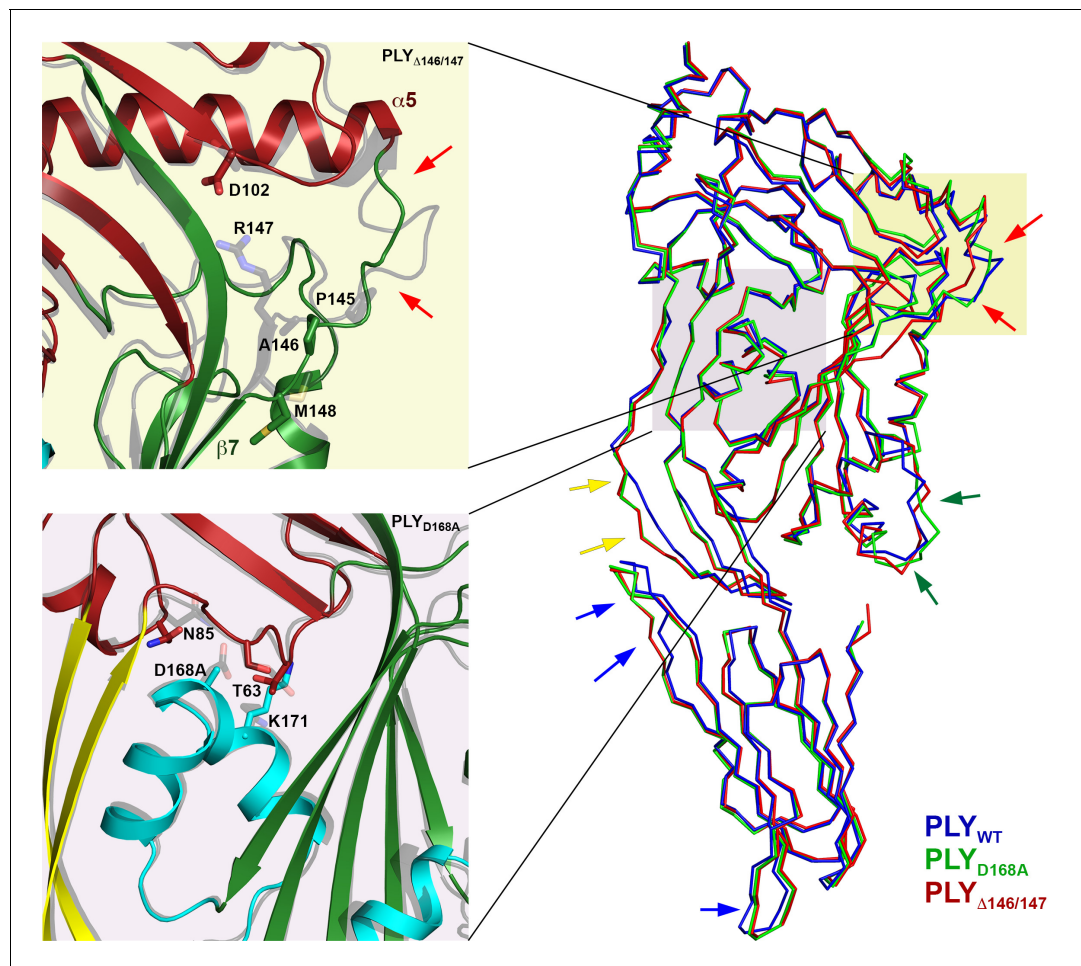


**Figure 8.** Location of functionally important PLY residues. (A) Ala146 and Arg147 in the loop that induces refolding of the last  $\beta$ -strand in the central D3  $\beta$ -sheet into helix  $\alpha$ 13a in the late prepore and pore complex. Deletion of both residues renders the toxin inactive. (B) In the pore complex, Asp168 near the end of one long trans-membrane  $\beta$ -hairpin (HP1) forms a salt bridge with Lys271 in the other trans-membrane  $\beta$ -hairpin (HP2) of the adjacent monomer. Replacing Asp168 by alanine inhibits membrane insertion. (C)  $\alpha$ -carbon traces in the x-ray structures of PLY<sub>WT</sub> (pdb 5aod), PLY<sub>Δ146/147</sub> (pdb 5aof), and PLY<sub>D168A</sub> (pdb 5aof). Minor differences between wildtype and mutant structures are visible in the loop regions of D4 (blue arrows); D2 (yellow arrows) and HB2 (green arrows). In PLY<sub>Δ146/147</sub>, one loop connecting D1 to D3 is also slightly different (red arrows).

DOI: 10.7554/eLife.23644.019

**Table 1.** Data collection and refinement statistics.

	PLY <sub>D168A</sub> (pdb-id 5aoc)	PLY <sub>A146/147</sub> (pdb-id 5aof)
<i>Data collection</i>		
Beamline	PXII @ Swiss Light Source x10sa	
Resolution (Å)	40–2.5 (2.6–2.5)	40–2.45 (2.55–2.45)
Wavelength (Å)	0.9786	0.978
Space group	<i>P</i> 2 <sub>1</sub>	<i>P</i> 2 <sub>1</sub> 2 <sub>1</sub> 2 <sub>1</sub>
<i>Cell dimensions</i>		
<i>a</i> , <i>b</i> , <i>c</i> (Å)	160.86 24.66 208.35	24.73 163.5 207.8
$\alpha$ , $\beta$ , $\gamma$ (°)	90, 90.26, 90	90, 90, 90
Total reflections	316531 (30235)	137706 (13089)
Unique reflections	59222 (5685)	29722 (2937)
Multiplicity	5.3 (5.3)	4.6 (4.5)
Completeness (%)	99 (100)	91 (94)
Mean <i>I</i> / $\sigma$ <i>I</i>	8.1 (1.4)	9.1 (1.2)
Wilson B-factor	46.75	45.05
<i>R</i> <sub>pim</sub>	0.08 (0.593)	0.07 (0.607)
CC*	0.998 (0.887)	0.999 (0.792)
<i>Refinement</i>		
Reflections used in refinement	59207 (5683)	29718 (2936)
Reflections in test set	2962 (285)	1486 (147)
<i>R</i> <sub>work</sub> / <i>R</i> <sub>free</sub> (%)	22.25/24.98 (32.9/33.7)	20.87/23.44 (33.23/34.37)
CC(work)/CC(free)	0.946/0.934 (0.769/0.737)	0.955/0.930 (0.626/0.567)
Average B-Factor (Å <sup>2</sup> )	72.5	64.3
No. atoms in AU	7878	4008
Protein	7724	3856
Water	154	152
r.m.s. deviations:		
Bond lengths (Å)	0.003	0.03
Bond angles (°)	0.72	0.69
Ramachandran favored (%)	96	96
Ramachandran allowed (%)	3.6	3.1
Ramachandran outliers (%)	0.5	0.8

Note: Values for the highest resolution shell are shown in parentheses

DOI: [10.7554/eLife.23644.020](https://doi.org/10.7554/eLife.23644.020)

protein regions that are promising targets for drug development. Drugs that interfere with these interactions would render the toxin ineffective, and the bacteria that produce it non-pathogenic.

## Discussion

With the ongoing resolution revolution in cryoEM (Kühlbrandt, 2014), structures of macromolecular assemblies can now be determined at high resolution without crystals. This is proving especially useful for membrane proteins and membrane protein complexes (Allegretti et al., 2015; Gu et al., 2016; Hahn et al., 2016; Letts et al., 2016; Liao et al., 2013), which tend to be unstable and flexible, and often do not crystallize. In the case of CDC pore complexes, structure determination represents a particular challenge, because they consist of variable numbers of 30 to 50 monomers

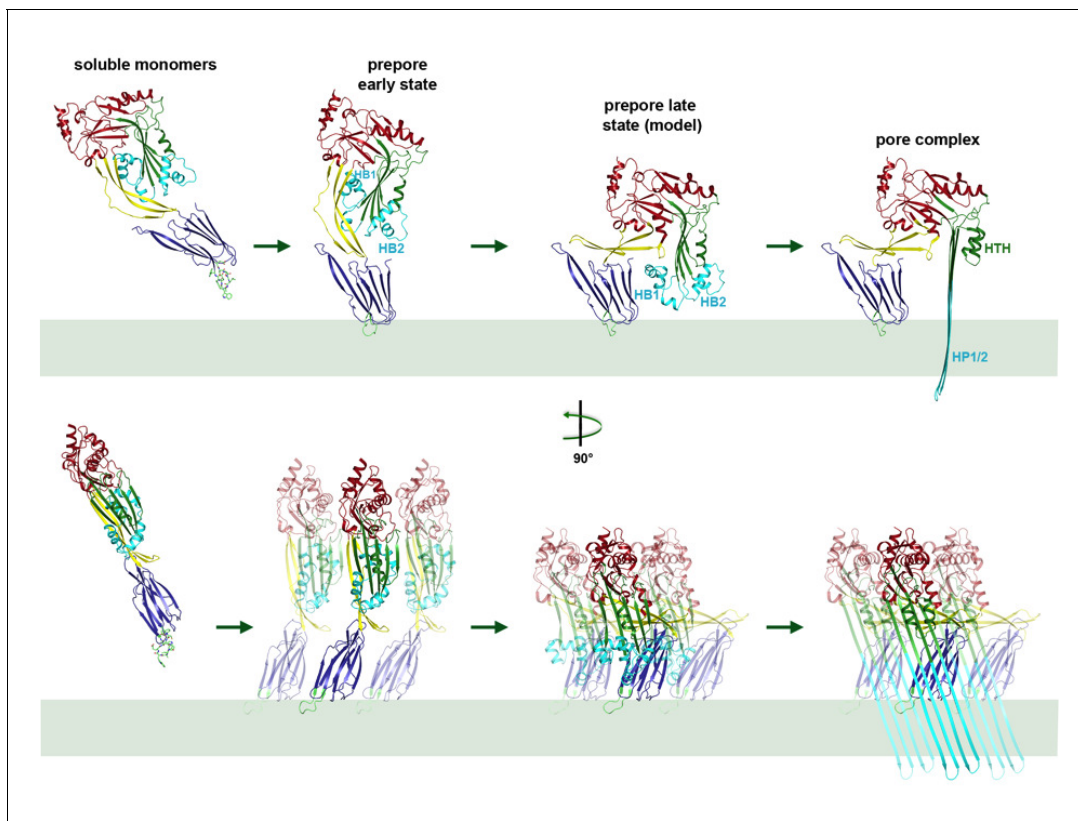
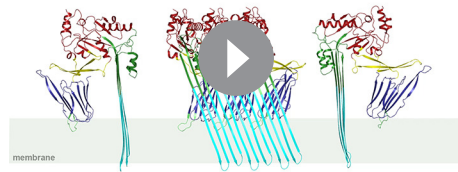


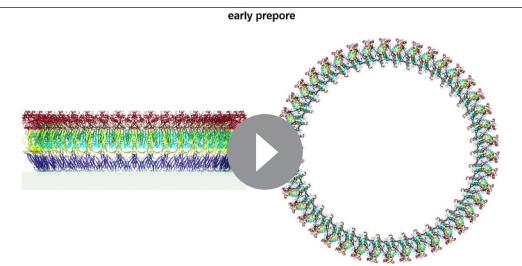
**Figure 9.** Mechanism of membrane insertion and pore formation. Stepwise conformational changes of PLY toxin during pore formation shown for one monomer (above, side view) and for three neighbouring monomers (below, view from the pore centre). In the first step, soluble PLY monomers attach to the surface of cholesterol-containing cell membranes via the conserved D4 undecapeptide (**Figure 2C**) to form circular oligomers of the early prepoire. A  $90^\circ$  rotation of D2 moves D1 and D3 towards the membrane in the late prepoire. Helix bundles HB1 and HB2 are poised above the membrane surface to refold into  $85 \text{ \AA}$   $\beta$ -hairpins HP1 and HP2. In the final step of pore formation, both hairpins traverse the hydrophobic membrane core and assemble into a 168-strand,  $260 \text{ \AA}$   $\beta$ -barrel. Reorganization of the PLY monomer exposes numerous charges on the inside of the  $\beta$ -barrel (**Figure 4**) that would destabilize the lipid bilayer and repel membrane lipids, resulting in pore opening and cell lysis.

DOI: 10.7554/eLife.23644.021

(Dang et al., 2005; Shatursky et al., 1999; Shepard et al., 1998), and hence are intrinsically inhomogeneous. This fact has so far precluded structure determination of the membrane-attached or membrane-inserted form at high resolution. By a rigorous screen of the detergents used for solubilisation and purification of the pore complex from cholesterol-containing liposomes we were able to isolate a suitably homogenous population. Exchanging the detergent against amphipols appeared to stabilize rings of uniform size, as an important prerequisite for high-resolution single-particle cryoEM. The number of monomers in the amphipol-stabilized complexes was higher than in the prepoires or the pores imaged by cryoET, even though the liposomes were prepared in the same way. This means that either the number of subunits in the ring varies from one liposome preparation to another, or that the rings rearrange into a more stable form upon detergent solubilisation, which we consider more likely. Interestingly, an earlier, low-resolution cryoEM structure of PLY pores and prepoires in lipid bilayers deduced that there were  $31 \pm 3$  subunits in the prepoire and 38 or 44 in the pore complex (Tilley et al., 2005), in good agreement with our findings. Since the PLY pores in our subtomogram averages were smaller, consisting of 34 rather than 42 subunits, it seems that the rings can grow in the membrane by incorporating further subunits. Apparently, complexes of 42 monomers are more stable than both larger and smaller rings. The inherent variability in ring size restricts the number of particles that can be averaged in any one class. Moreover, the large ring-shaped assemblies are easily distorted and rarely, if ever, perfectly circular, which limits the accuracy to which they can be aligned by image processing. Both factors constrain the attainable resolution of the cryoEM reconstruction.



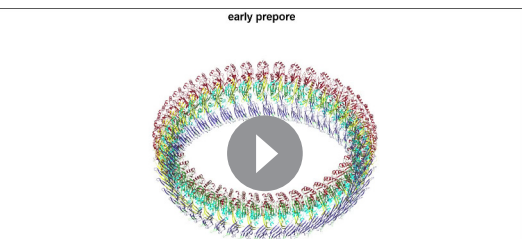
**Video 2.** Mechanism of pneumolysin pore formation. (1) Soluble PLY monomers attach to cholesterol-rich membranes by the cholesterol-binding undecapeptide (light green) of domain D4 (blue) and oligomerize into rings. For simplicity, only three ring subunits are shown. (2) Domain D2 (yellow) rotates by 90°, bringing domain D3 (green) with its two helix bundles (cyan) close to the membrane surface. (3) The helix bundles insert into the membrane and unfold into two trans-membrane 85 Å  $\beta$ -hairpins.  $\beta$ -hairpins of the 42 subunits in the ring merge into one large 168-strand  $\beta$ -barrel, which perforates the membrane.  
DOI: [10.7554/eLife.23644.022](https://doi.org/10.7554/eLife.23644.022)



**Video 3.** Model of conformational changes in an entire ring of 42 PLY monomers from early prepore to late prepore to pore, seen from the side and from above.  
DOI: [10.7554/eLife.23644.023](https://doi.org/10.7554/eLife.23644.023)

Earlier cryoEM work, AFM and FRET studies have described the vertical height change of the prepore upon membrane insertion in terms of a collapse or unfolding of D2 (Czajkowsky *et al.*, 2004; Ramachandran *et al.*, 2005; Tilley *et al.*, 2005). Our atomic model of the pore complex now shows that this change is due to a rigid-body rotation of D2, in which the structure of the domain remains intact. Time-lapse AFM of PLY and listeriolysin (LLO) on planar membranes indicated that the vertical height change is not directly linked to pore formation (Mulvihill *et al.*, 2015; van Pee *et al.*, 2016), in line with a mechanism that involves two different prepore states that we refer to as the early and late prepore. Our model of the late prepore monomer (Figure 9) is an intermediate between the x-ray structure of the soluble form and the cryoEM structure of the membrane-inserted form. The 5-stranded central  $\beta$ -sheet in the crystal structure of D3 fits into the cryoEM map of the early prepore complex without any modification, but the late prepore model indicates a potential steric clash between the short  $\beta$ -strand in the central  $\beta$ -sheet of D3 and the adjacent monomer. The pivotal role of the loop that contains residues 145–147 connecting helix  $\alpha$ 5 of D1 to  $\beta$ 7 of  $\beta$ -hairpin one is underlined by mutant PLY $_{\Delta 146/147}$  that was completely inactive (Kirkham *et al.*, 2006) and did not even bind to liposomes (Figure 7A). The detachment of PLY $_{D168A}$  rings indicates that the mutant does not insert into the membrane as easily as PLY $_{WT}$  to form pores. We have shown by time-lapse AFM that pore formation is irreversible (van Pee *et al.*, 2016). Therefore the rings that become detached from the membrane are prepores, not pores.

In earlier models of pore formation, the conserved domain D4 (Figure 3) was thought to be important for toxin targeting, receptor recognition and binding to cholesterol-containing membranes (Farrand *et al.*, 2010; Ramachandran *et al.*, 2002; Soltani *et al.*, 2007a, 2007b), whereas oligomer formation was mainly attributed to intermolecular interactions via D1 and D3 (Lawrence *et al.*, 2015; Ramachandran *et al.*, 2002). It has however been shown that D4 of streptolysin, pyolysin and LLO can oligomerise by itself on cholesterol crystals (Harris *et al.*, 2011; Weis and Palmer, 2001) or erythrocyte ghosts (Köster *et al.*, 2014). Our cryoEM structure confirms that D4 can indeed



**Video 4.** Oblique view of PLY ring inserting into the membrane.  
DOI: [10.7554/eLife.23644.024](https://doi.org/10.7554/eLife.23644.024)

play a role in oligomer formation through intra- and intermolecular interactions of its loops (**Figure 2—figure supplements 2 and 3**). Loop  $\beta$ 22/23 and the conserved undecapeptide loop with Trp433 at its tip appear to interact with loop  $\beta$ 18/19 of the neighbouring monomer, thereby stabilizing the pore complex by inter- and intramolecular interactions (**Figure 2—figure supplements 2 and 3**).

The surface charge distribution on the toxin monomers is critical for CDC activity. Modification of surface charges affects ring formation, as we demonstrated by mutagenesis both for LLO (**Köster et al., 2014**) and PLY (**van Pee et al., 2016**). The alternating positive and negative charges of the HTH motif (**Figure 5D**) and the positive charges at the tips of the  $\beta$ -hairpins (**Figure 5E,F**) demonstrate the importance of charge complementarity for PLY ring formation. A similar HTH motif was found in the 8 Å cryoEM map of poly-C9 component of the human membrane attack complex (**Dudkina et al., 2016**). This HTH motif was already present in the soluble monomer of the C6 component (**Aleshin et al., 2012**). As in PLY, the HTH in the poly-C9 pore forms an  $\alpha$ -barrel that determines the effective pore diameter.

Together with the x-ray structure of the soluble form, our cryoEM structures of the pore and prepore explain the step-by-step process of membrane insertion and pore formation in near-atomic detail. Movies showing the transition from the soluble monomer to the pore complex via the intermediate stages of the early and late prepore illustrate the complete mechanism of pore formation (**Videos 2–4**). In the early prepore, PLY monomers assemble side by side into rings on the membrane surface. In the late prepore, the D3 helices are poised for re-folding immediately above membrane surface. Helix unfolding may be a stochastic yet cooperative event, such that the spontaneous transition of one monomer triggers the refolding of its neighbours in the ring, comparable to a zipper. As the 168-strand  $\beta$ -barrel assembles in the membrane, the charged patches on its inside surface would repel any trapped hydrophobic lipid. Most likely the lipid is pushed out of the nascent pore by successively inserted toxin monomers, rather than being ejected in the form of micelles or small vesicles, as has been proposed for suliyisin (**Leung et al., 2014**). Upon pore formation, the membrane potential collapses, the cytoplasm leaks out and the cell dies.

The mechanism of membrane insertion by rearrangement of the conserved domains 1–4 is likely to be the same for all CDCs. Therefore, compounds that interfere with refolding and membrane insertion of soluble monomers would prevent infection by *Streptococcus pneumoniae* and other CDC-producing Gram-positive bacteria that attack human cells with similar pore-forming toxins. The 4.5 Å cryoEM structure of the PLY pore complex thus paves the way towards the design of new drugs that inhibit pore formation as a promising approach towards combatting infections by dangerous and wide-spread Gram-positive pathogens.

## Materials and methods

### Protein expression and purification

The gene coding for N-terminal His<sub>6</sub>-tagged PLY was inserted into the pET15b vector. *E. coli* BL21 (DE3) cells transformed with the expression plasmid were grown in TB medium containing 50  $\mu\text{g} \cdot \text{ml}^{-1}$  ampicillin. Protein expression was induced with 1 mM isopropyl- $\beta$ -D-1-thiogalactopyranoside upon reaching an optical density of one at 600 nm. After 4 hr at 37°C the cells were pelleted, resuspended in Buffer A (50 mM Tris pH 7.0, 150 mM NaCl, 30 mM Imidazole, 5 mM  $\beta$ -mercaptoethanol) and disrupted with a Microfluidizer (M-110L, Microfluidics Corp., Newton, MA). PLY was purified on a HisTrap FF column, equilibrated with Buffer A. The protein was eluted in Buffer A containing 300 mM imidazole. Protein fractions were pooled and diluted in 50 mM Tris pH 7.0, 5 mM  $\beta$ -mercaptoethanol to a final NaCl concentration of 50 mM. The His<sub>6</sub>-tag was removed by overnight cleavage with thrombin at 4°C. The protein was further purified on a HiTrap Q FF ion-exchange column equilibrated in Buffer B (50 mM Tris-HCl pH 7.0, 50 mM NaCl, 5 mM  $\beta$ -mercaptoethanol). PLY was eluted in Buffer B containing 170 mM NaCl. Protein fractions were pooled, concentrated to 10  $\text{mg} \cdot \text{ml}^{-1}$  and stored at  $-80^\circ\text{C}$ .

### Site-directed mutagenesis and hemolysis assays

Site-directed mutagenesis was performed with the QuikChange site-directed mutagenesis kit (Stratagene) according to the manufacturer's instructions with the wildtype construct as a template. All

constructs were verified by nucleotide sequencing. The hemolytic activity of PLY was determined by lysis of sheep red blood cells (SRBC) (Darji et al., 1995). Purified protein was serially diluted in hemolysis buffer (50 mM sodium phosphate pH 6.6, 150 mM NaCl, 5 mM DTT, 0.1% (v/v) BSA) in final volumes of 50  $\mu$ l and incubated for 30 min at 37°C with 50  $\mu$ l of a suspension of SRBC ( $10^8$  ml<sup>-1</sup>). Release of hemoglobin was monitored by recording the absorbance at 405 nm. The amount of toxin necessary to lyse 50% of erythrocytes was determined and expressed as percentage of the value for PLY<sub>WT</sub>. The absorbance upon incubation with 1% Triton-X100 was used as reference value for 100% lysis of erythrocytes. Three independent measurements were performed for each PLY mutant.

### Liposome preparation and amphipol stabilization

A lipid mixture containing 70 mol-% di-oleyl phosphatidyl choline (DOPC) and 30 mol-% cholesterol in chloroform was dried under a constant nitrogen stream. The lipid film was taken up in 50 mM Tris-HCl pH 7.0, 150 mM NaCl, 5 mM  $\beta$ -mercaptoethanol at a final concentration of 10 mg  $\cdot$  ml<sup>-1</sup> and stirred overnight at room temperature. After three freeze-thaw cycles (liquid nitrogen, 37°C), the suspension was passed through an extruder to obtain unilamellar ~200 nm liposomes. The extruded liposomes were flash-frozen in liquid nitrogen and stored at -20°C. The liposome suspension was incubated with PLY at a final lipid-to-protein ratio of 1:2 (wt/wt) at 37°C for 30 min. For the preparation of PLY pore complexes, the proteoliposomes were solubilized at a final concentration of 0.56% Cymal-6 at room temperature overnight. Amphipol A8-35 was added in fivefold molar excess and the suspension was incubated for 30 min at room temperature. Detergent was removed by dialysis against 50 mM Tris-HCl pH 7.0, 150 mM NaCl, 5 mM  $\beta$ -mercaptoethanol at room temperature for 72 hr.

### Specimen preparation for negative-stain EM

PLY mutant pores were compared to wildtype protein formed on planar lipid layers or cholesterol-containing liposomes prepared as above. The liposome mixture was diluted to a final concentration of 0.5 mg  $\cdot$  ml<sup>-1</sup> and 25  $\mu$ g  $\cdot$  ml<sup>-1</sup> PLY was added. Planar lipid bilayers and PLY were incubated in Teflon well plates. 25  $\mu$ g  $\cdot$  ml<sup>-1</sup> PLY in reaction buffer (150 mM NaCl, 50 mM Tris-HCl pH 7.0, 5 mM  $\beta$ -mercaptoethanol) was transferred into a well and overlaid with a droplet of a 0.5 mg  $\cdot$  ml<sup>-1</sup> DOPC/cholesterol solution (1:1 molar ratio) in chloroform. Planar lipid layers formed upon chloroform evaporation. Wells were incubated for 30 min at 37°C, after which PLY-containing membranes were transferred to EM grids and stained with 1% (wt/vol) uranyl acetate. Negatively stained specimens were examined in an FEI Tecnai Spirit electron microscope at an acceleration voltage of 120 kV. Images were recorded on a 2 K Gatan CCD camera at a magnification of 25,000x–45,000x and ~1.0–1.5  $\mu$ m underfocus.

### Single-particle cryoEM and image processing

Amphipol-solubilized PLY pores were diluted to a final concentration of 1 mg  $\cdot$  ml<sup>-1</sup>. A 3  $\mu$ l aliquot was applied to freshly glow-discharged R2/2 holey carbon grids (Quantifoil Micro Tools, Jena, Germany), blotted for 3 to 4 s at 10°C and 100% humidity in a Vitrobot Mark IV (FEI). Preferential orientation of toxin rings on the air-water interface was overcome by carbon backing. Dose-fractionated 6.0 s movies of 30 frames with an electron dose of 1.02 e<sup>-</sup>  $\cdot$  (Å<sup>2</sup>  $\cdot$  frame)<sup>-1</sup> were recorded after coma-free alignment (Allegretti et al., 2014) with an FEI Polara electron microscope operating at 300 kV with 0.5–3.6  $\mu$ m underfocus and a specimen pixel size of 1.4 Å on a K2 Summit direct electron detection camera (Gatan, Pleasanton, USA) operating in counting mode with an energy filter slit of 20 eV. Movie frames were corrected for beam-induced motion with Motioncorr (Li et al., 2013) and again with UNBLUR (Grant and Grigorieff, 2015), which also applied a dose-dependent filter. The contrast transfer function of each image was determined using CTFFIND3 (Mindell and Grigorieff, 2003). A total of 12308 particle images were hand-picked from 983 micrographs in RELION 1.3 or 1.4 (Scheres, 2012, 2015) and extracted into 360-pixel boxes. Initial 2D classification indicated that rings with 42-fold symmetry were most common, although rings with different symmetries were also present. For 3D classification in RELION, the pore structure of suliyisin (EMD-2983) low-pass filtered to 50 Å was used as a reference. For the next processing step, the unsymmetrized low-resolution PLY map was used as the reference. Subsequent 3D classification yielded three classes, of which two



had clear 42-fold symmetry. Rings that were distorted, damaged or of different size were sorted out at the 3D classification stage. A total of 6461 particles from 3D classes of 42-fold symmetry were auto-refined in RELION. A B-factor of  $-175 \text{ \AA}^2$  for map sharpening was determined using the modulation transfer function of the K2 Summit detector. The resolution of the processed data after B-factor sharpening was  $4.5 \text{ \AA}$  ( $\text{FSC}_{0.143}$ ), with an estimated orientation accuracy of  $0.75^\circ$ . Local resolution was assessed with RELION 2.0 (Kimanius et al., 2016).

### CryoET of PLY prepores and pores

Preformed liposomes were incubated with PLY ( $1 \text{ mg} \cdot \text{ml}^{-1}$ ) at room temperature for 30 min to obtain prepores, or at  $37^\circ\text{C}$  for 30–180 min to obtain pores. For cryoET the liposomes were diluted 1:3 with buffer (150 mM NaCl, 50 mM Tris-HCl pH 7.0, 5 mM  $\beta$ -mercaptoethanol) and then 1:1 with 6 nm gold particles conjugated with protein A (Aurion) as fiducial markers. Samples of  $3 \mu\text{l}$  were applied to glow-discharged Quantifoil EM grids (R2/2, Cu 300 mesh), excess liquid was blotted off with filter paper (Whatman #4) and samples were vitrified by plunge-freezing into liquid ethane (Dubochet et al., 1988). Single-axis tilt series were typically collected from  $-62^\circ$  to  $+62^\circ$  at  $2^\circ$  increments and 3–4  $\mu\text{m}$  underfocus with a total electron dose of  $60\text{--}80 \text{ e}^- \cdot \text{\AA}^{-2}$ , on a Tecnai Polara electron microscope equipped with a field emission gun operating at 300 kV (FEI, Hillsboro, OR), a post-column energy filter (GIF Quantum, Gatan) and a K2 summit direct electron detector (Gatan). Images were recorded in counting mode with a pixel size of 0.35 nm. Tilt series were CTF-corrected, binned  $2 \times 2$  and aligned. Tomographic volumes were generated by weighted back projection in IMOD (Kremer et al., 1996).

### Sub-tomogram averaging

For particle picking and initial rounds of sub-tomogram averaging (Frangakis and Hegerl, 2001), tomograms were filtered by nonlinear anisotropic diffusion to enhance contrast. Ring-shaped complexes were picked manually in 3dmod. A total of 752 prepore complexes and 2400 pore complexes were picked for averaging. Ring volumes were pre-aligned in one plane in  $2 \times 2$  binned unfiltered tomograms. All prepores had roughly the same size and shape and were averaged in PEET (Nicastro et al., 2006). The average volume was used as an initial reference for symmetry determination by sub-tomogram averaging with IMOD (Kremer et al., 1996). Symmetries of 42-fold or lower were applied to each prepore volume on a trial-and-error basis. Volumes were aligned and averaged in an iterative process, which converged within about 15 iterations on an average volume with clear 34-fold symmetry. The best 70% of the prepore volumes contributed to the final average, in which 34 PLY monomers were resolved in the ring.

Pore complexes were separated into seven classes according to their shape and diameter by principal component analysis and clusterPCA in IMOD (Kremer et al., 1996). The best class with 844 pore complexes was used for further processing as described above. In the final pore complex average, individual subunits were clearly distinguished in one third of the ring, indicating some heterogeneity of ring size and symmetry (Figure 5B). The number of PLY monomers in the pore was determined as 34 from the angular distance between distinct subunits in the average volume and the ring diameter. As for the prepores, all averaging steps were performed in PEET (Nicastro et al., 2006). The resolution at  $\text{FSC}_{0.5}$  was  $27 \text{ \AA}$  for the pore and  $22 \text{ \AA}$  for the prepore (Figure 6c). At  $\text{FSC}_{0.3}$ , the resolution of the pore and prepore complex would be  $21 \text{ \AA}$  and  $20 \text{ \AA}$ , respectively.

### Model building and analysis

Model building was performed in COOT (Emsley and Cowtan, 2004) based on the x-ray structure of the water-soluble PLY monomer (pdb 5a0d; (van Pee et al., 2016)). Initially, individual domains in the x-ray structure of soluble PLY were fitted manually into the cryoEM map as rigid bodies using COOT. Refolded or flexible protein regions were re-fitted manually, followed by geometry regularization in COOT. The complete backbone of PLY was traced in the pore complex map. Densities of bulky side chains were observed in well-ordered regions. The transmembrane  $\beta$ -hairpins, which form upon unfolding of HB1 and HB2 in domain 3 were readily fitted to the map density. The pore model with 42 subunits was generated in UCSF Chimera (Pettersen et al., 2004). Sub-tomogram average maps of the PLY prepore were fitted in UCSF Chimera with the x-ray structures of the PLY monomer (pdb 5cr6; [Marshall et al., 2015]). Sub-tomogram averages of the pore complex were fitted with

the cryoEM structure of the membrane-inserted form. Figures were drawn with PyMol (*Schrödinger, 2015*). FSC curves of model versus map were calculated using the EMAN package (*Tang et al., 2007*).

## Crystallization, data collection, structure determination, and refinement

Initial crystallization trials were carried out with a protein concentration of  $8 \text{ mg} \cdot \text{ml}^{-1}$  (PLY<sub>D168A</sub>) or  $10 \text{ mg} \cdot \text{ml}^{-1}$  (PLY<sub>Δ146/147</sub>) after addition of glycerol to a final concentration of 10% in 96-well plates by vapour diffusion. 300 nl of protein solution were mixed with 300 nl of a commercially available crystallization solution (PGA Screen from Molecular Dimensions, JB Screen Classics I from Jena Bioscience, and Classics I Suite from Qiagen) in a pipetting robot (Mosquito, TTP Labtech). Hanging drops were incubated over 100 μl of reservoir solution at 18°C. Initial crystals hits were refined by varying the protein-to-reservoir ratio with a drop volume of 3 μl, incubated over 500 μl reservoirs at 18°C in 24-well plates. PLY<sub>D168A</sub> crystals grew after one day at 18°C in a 3 μl drop of 1.5 μl protein solution ( $8 \text{ mg} \cdot \text{ml}^{-1}$  in 10% glycerol) and 1.5 μl of reservoir solution (0.1 M sodium cacodylate pH 6.5, 1% PGA-LM, 0.2 M potassium bromide and 0.2 M potassium thiocyanate). PLY<sub>Δ146/147</sub> crystals grew in a few days at 18°C in a 3 μl drop of 2.0 μl protein solution ( $10 \text{ mg} \cdot \text{ml}^{-1}$  in 10% glycerol) and 1.0 μl of reservoir solution (0.1 M imidazole pH 6.5 and 1.2 M sodium acetate). Crystals were transferred to reservoir solution as a cryo-protectant and flash-frozen in liquid nitrogen. Data were collected at beamline PXII (Paul Scherrer Institute, Villigen, Switzerland) under a constant stream of cold nitrogen gas (100 K). Data processing, integration and scaling was performed with the XDS package (*Kabsch, 1993*). Structures of the PLY mutants were solved by molecular replacement with PLY<sub>WT</sub> (pdb-id 4AOD) as a search model using PHASER (*McCoy, 2007*) in the CCP4 software package (*Collaborative Computational Project, Number 4, 1994*). The initial electron density map was improved by cycles of density modification, automatic model building in RESOLVE (*Terwilliger, 2004*) and refinement by REFMAC (*Murshudov et al., 1997*). The model was subjected to iterative rounds of rebuilding into 2F<sub>o</sub>-F<sub>c</sub> and F<sub>o</sub>-F<sub>c</sub> maps using COOT (*Emsley and Cowtan, 2004*) and refined with the phenix.refine subroutine in the PHENIX program suite (*Zwart et al., 2008*). Data collection, refinement, and model statistics are summarized in **Table 1**. Figures were generated with PyMOL (*Schrödinger, 2015*).

## Accession numbers

The cryoEM density map has been deposited in the Electron Microscopy Data Bank under the accession number EMD-4118. The structure coordinates have been deposited in the protein data bank under accession number 5LY6 (PLY pore complex), 5AOE (PLY<sub>D168A</sub>) and 5AOF (PLY<sub>Δ146/147</sub>)

## Acknowledgements

We thank Janet Vonck for discussion and advice on image processing, Sabine Häder and Heidi Betz for technical assistance, Sebastian Schaupp for help with screening solubilisation conditions and negative-stain EM, and Juan Castillo for computer support. This work was funded by the Max Planck Society.

---

## Additional information

### Competing interests

WK: Reviewing editor, *eLife*. The other authors declare that no competing interests exist.

### Funding

Funder	Grant reference number	Author
Max-Planck-Gesellschaft	DepartmentSB	Katharina van Pee Alexander Neuhaus Edoardo D'Imprima Deryck J Mills Werner Kühlbrandt Özkan Yildiz

The funders had no role in study design, data collection and interpretation, or the decision to submit the work for publication.

### Author contributions

KvP, Data curation, Investigation, Methodology, Writing—original draft, Performed biochemical experiments, Carried out single-particle cryoEM and processing, Interpreted the data and wrote the paper; AN, Investigation, Methodology, Performed cryo-tomography and sub-tomogram averaging and analysis of data; ED, Investigation, Methodology, Interpreted the data and wrote the paper; DJM, Investigation, Methodology, Devised the cryoEM data collection strategy; WK, Resources, Formal analysis, Funding acquisition, Writing—review and editing, Interpreted the data and wrote the paper; ÖY, Conceptualization, Data curation, Formal analysis, Supervision, Validation, Investigation, Visualization, Methodology, Writing—original draft, Project administration, Writing—review and editing, Initiated and directed the project, Interpreted the data and wrote the paper

### Author ORCIDs

Werner Kühlbrandt, <http://orcid.org/0000-0002-2013-4810>

Özkan Yildiz, <http://orcid.org/0000-0003-3659-2805>

## Additional files

### Major datasets

The following datasets were generated:

Author(s)	Year	Dataset title	Dataset URL	Database, license, and accessibility information
van Pee K, Neuhaus A, D'Imprima E, Mills DJ, Kuehlbrandt W, Yildiz O	2016	CryoEM structure of the membrane pore complex of Pneumolysin at 4.5Å	<a href="https://www.ebi.ac.uk/pdbe/entry/pdb/5ly6">https://www.ebi.ac.uk/pdbe/entry/pdb/5ly6</a>	Publicly available at the EMBL-EBI Protein Data Bank (accession no: 5LY6)
van Pee K, Neuhaus A, D'Imprima E, Mills DJ, Kuehlbrandt W, Yildiz O	2016	CryoEM structure of the membrane pore complex of Pneumolysin at 4.5Å	<a href="http://www.ebi.ac.uk/pdbe/entry/emdb/EMD-4118">http://www.ebi.ac.uk/pdbe/entry/emdb/EMD-4118</a>	Publicly available at the EMBL-EBI Protein Data Bank (accession no: EMD-4118)
van Pee K, Yildiz O	2016	Crystal structure of pneumolysin deletion mutant Delta146_147	<a href="http://www.rcsb.org/pdb/explore/explore.do?structureId=5AOF">http://www.rcsb.org/pdb/explore/explore.do?structureId=5AOF</a>	Publicly available at the RCSB Protein Data Bank (accession no: 5AOF)
van Pee K, Yildiz O	2016	Crystal structure of pneumolysin D168A mutant	<a href="http://www.rcsb.org/pdb/explore/explore.do?structureId=5AOE">http://www.rcsb.org/pdb/explore/explore.do?structureId=5AOE</a>	Publicly available at the RCSB Protein Data Bank (accession no: 5AOE)

The following previously published dataset was used:

Author(s)	Year	Dataset title	Dataset URL	Database, license, and accessibility information
van Pee K, Yildiz O	2016	Crystal structure of wild type pneumolysin	<a href="http://www.rcsb.org/pdb/explore/explore.do?structureId=5aod">http://www.rcsb.org/pdb/explore/explore.do?structureId=5aod</a>	Publicly available at the RCSB Protein Data Bank (accession no: 5AOD)

## References

- Aleshin AE, Schraufstatter IU, Stec B, Bankston LA, Liddington RC, DiScipio RG. 2012. Structure of complement C6 suggests a mechanism for initiation and unidirectional, sequential assembly of membrane attack complex (MAC). *Journal of Biological Chemistry* **287**:10210–10222. doi: [10.1074/jbc.M111.327809](https://doi.org/10.1074/jbc.M111.327809), PMID: [22267737](https://pubmed.ncbi.nlm.nih.gov/22267737/)
- Allegretti M, Klusch N, Mills DJ, Vonck J, Kühlbrandt W, Davies KM. 2015. Horizontal membrane-intrinsic  $\alpha$ -helices in the stator a-subunit of an F-type ATP synthase. *Nature* **521**:237–240. doi: [10.1038/nature14185](https://doi.org/10.1038/nature14185), PMID: [25707805](https://pubmed.ncbi.nlm.nih.gov/25707805/)

- Allegretti M**, Mills DJ, McMullan G, Kühlbrandt W, Vonck J. 2014. Atomic model of the F420-reducing [NiFe] hydrogenase by electron cryo-microscopy using a direct electron detector. *eLife* **3**:e01963. doi: [10.7554/eLife.01963](https://doi.org/10.7554/eLife.01963), PMID: [24569482](https://pubmed.ncbi.nlm.nih.gov/24569482/)
- Althoff T**, Mills DJ, Popot JL, Kühlbrandt W. 2011. Arrangement of electron transport chain components in bovine mitochondrial supercomplex I1III2IV1. *The EMBO Journal* **30**:4652–4664. doi: [10.1038/emboj.2011.324](https://doi.org/10.1038/emboj.2011.324), PMID: [21909073](https://pubmed.ncbi.nlm.nih.gov/21909073/)
- Collaborative Computational Project, Number 4**. 1994. The CCP4 suite: programs for protein crystallography. *Acta Crystallographica. Section D, Biological Crystallography* **50**:760–763. doi: [10.1107/S0907444994003112](https://doi.org/10.1107/S0907444994003112), PMID: [15299374](https://pubmed.ncbi.nlm.nih.gov/15299374/)
- Czajkowsky DM**, Hotze EM, Shao Z, Tweten RK. 2004. Vertical collapse of a cytolysin prepore moves its transmembrane beta-hairpins to the membrane. *The EMBO Journal* **23**:3206–3215. doi: [10.1038/sj.emboj.7600350](https://doi.org/10.1038/sj.emboj.7600350), PMID: [15297878](https://pubmed.ncbi.nlm.nih.gov/15297878/)
- Dang TX**, Hotze EM, Rouiller I, Tweten RK, Wilson-Kubalek EM. 2005. Prepore to pore transition of a cholesterol-dependent cytolysin visualized by electron microscopy. *Journal of Structural Biology* **150**:100–108. doi: [10.1016/j.jsb.2005.02.003](https://doi.org/10.1016/j.jsb.2005.02.003), PMID: [15797734](https://pubmed.ncbi.nlm.nih.gov/15797734/)
- Darji A**, Chakraborty T, Niebuhr K, Tsonis N, Wehland J, Weiss S. 1995. Hyperexpression of listeriolysin in the nonpathogenic species *Listeria innocua* and high yield purification. *Journal of Biotechnology* **43**:205–212. doi: [10.1016/0168-1656\(95\)00138-7](https://doi.org/10.1016/0168-1656(95)00138-7), PMID: [8590646](https://pubmed.ncbi.nlm.nih.gov/8590646/)
- Dubochet J**, Adrian M, Chang JJ, Homo JC, Lepault J, McDowell AW, Schultz P. 1988. Cryo-electron microscopy of vitrified specimens. *Quarterly Reviews of Biophysics* **21**:129–228. doi: [10.1017/S0033583500004297](https://doi.org/10.1017/S0033583500004297), PMID: [3043536](https://pubmed.ncbi.nlm.nih.gov/3043536/)
- Dudkina NV**, Spicer BA, Reboul CF, Conroy PJ, Lukyanova N, Elmlund H, Law RH, Ekkel SM, Kondos SC, Goode RJ, Ramm G, Whisstock JC, Saibil HR, Dunstone MA. 2016. Structure of the poly-C9 component of the complement membrane attack complex. *Nature Communications* **7**:10588. doi: [10.1038/ncomms10588](https://doi.org/10.1038/ncomms10588), PMID: [26841934](https://pubmed.ncbi.nlm.nih.gov/26841934/)
- Emsley P**, Cowtan K. 2004. Coot: model-building tools for molecular graphics. *Acta Crystallographica Section D Biological Crystallography* **60**:2126–2132. doi: [10.1107/S0907444904019158](https://doi.org/10.1107/S0907444904019158), PMID: [15572765](https://pubmed.ncbi.nlm.nih.gov/15572765/)
- Farrand AJ**, LaChapelle S, Hotze EM, Johnson AE, Tweten RK. 2010. Only two amino acids are essential for cytolytic toxin recognition of cholesterol at the membrane surface. *PNAS* **107**:4341–4346. doi: [10.1073/pnas.0911581107](https://doi.org/10.1073/pnas.0911581107), PMID: [20145114](https://pubmed.ncbi.nlm.nih.gov/20145114/)
- Frangakis AS**, Hegerl R. 2001. Noise reduction in electron tomographic reconstructions using nonlinear anisotropic diffusion. *Journal of Structural Biology* **135**:239–250. doi: [10.1006/jsbi.2001.4406](https://doi.org/10.1006/jsbi.2001.4406), PMID: [11722164](https://pubmed.ncbi.nlm.nih.gov/11722164/)
- Gilbert RJ**. 2005. Inactivation and activity of cholesterol-dependent cytolysins: what structural studies tell us. *Structure* **13**:1097–1106. doi: [10.1016/j.str.2005.04.019](https://doi.org/10.1016/j.str.2005.04.019), PMID: [16084382](https://pubmed.ncbi.nlm.nih.gov/16084382/)
- Grant T**, Grigorieff N. 2015. Measuring the optimal exposure for single particle cryo-EM using a 2.6 Å reconstruction of rotavirus VP6. *eLife* **4**:e06980. doi: [10.7554/eLife.06980](https://doi.org/10.7554/eLife.06980), PMID: [26023829](https://pubmed.ncbi.nlm.nih.gov/26023829/)
- Gu J**, Wu M, Guo R, Yan K, Lei J, Gao N, Yang M. 2016. The architecture of the mammalian respirasome. *Nature* **537**:639–643. doi: [10.1038/nature19359](https://doi.org/10.1038/nature19359), PMID: [27654917](https://pubmed.ncbi.nlm.nih.gov/27654917/)
- Hahn A**, Parey K, Bublitz M, Mills DJ, Zickermann V, Vonck J, Kühlbrandt W, Meier T. 2016. Structure of a complete ATP synthase dimer reveals the molecular basis of inner mitochondrial membrane morphology. *Molecular Cell* **63**:445–456. doi: [10.1016/j.molcel.2016.05.037](https://doi.org/10.1016/j.molcel.2016.05.037), PMID: [27373333](https://pubmed.ncbi.nlm.nih.gov/27373333/)
- Harris JR**, Lewis RJ, Baik C, Pokrajac L, Billington SJ, Palmer M. 2011. Cholesterol microcrystals and cochleate cylinders: attachment of pyolysin oligomers and domain 4. *Journal of Structural Biology* **173**:38–45. doi: [10.1016/j.jsb.2010.07.010](https://doi.org/10.1016/j.jsb.2010.07.010), PMID: [20682347](https://pubmed.ncbi.nlm.nih.gov/20682347/)
- Hotze EM**, Tweten RK. 2012. Membrane assembly of the cholesterol-dependent cytolysin pore complex. *Biochimica Et Biophysica Acta (BBA) - Biomembranes* **1818**:1028–1038. doi: [10.1016/j.bbame.2011.07.036](https://doi.org/10.1016/j.bbame.2011.07.036), PMID: [21835159](https://pubmed.ncbi.nlm.nih.gov/21835159/)
- Kabsch W**. 1993. Automatic processing of rotation diffraction data from crystals of initially unknown symmetry and cell constants. *Journal of Applied Crystallography* **26**:795–800. doi: [10.1107/S0021889893005588](https://doi.org/10.1107/S0021889893005588)
- Kimanius D**, Forsberg BO, Scheres SH, Lindahl E. 2016. Accelerated cryo-EM structure determination with parallelisation using GPUs in RELION-2. *eLife* **5**:e18722. doi: [10.7554/eLife.18722](https://doi.org/10.7554/eLife.18722), PMID: [27845625](https://pubmed.ncbi.nlm.nih.gov/27845625/)
- Kirkham LA**, Kerr AR, Douce GR, Paterson GK, Dilts DA, Liu DF, Mitchell TJ. 2006. Construction and immunological characterization of a novel nontoxic protective pneumolysin mutant for use in future pneumococcal vaccines. *Infection and Immunity* **74**:586–593. doi: [10.1128/IAI.74.1.586-593.2006](https://doi.org/10.1128/IAI.74.1.586-593.2006), PMID: [16369015](https://pubmed.ncbi.nlm.nih.gov/16369015/)
- Kremer JR**, Mastrorade DN, McIntosh JR. 1996. Computer visualization of three-dimensional image data using IMOD. *Journal of Structural Biology* **116**:71–76. doi: [10.1006/jsbi.1996.0013](https://doi.org/10.1006/jsbi.1996.0013), PMID: [8742726](https://pubmed.ncbi.nlm.nih.gov/8742726/)
- Köster S**, van Pee K, Hudel M, Leustik M, Rhinow D, Kühlbrandt W, Chakraborty T, Yildiz Ö. 2014. Crystal structure of listeriolysin O reveals molecular details of oligomerization and pore formation. *Nature Communications* **5**:3690. doi: [10.1038/ncomms4690](https://doi.org/10.1038/ncomms4690), PMID: [24751541](https://pubmed.ncbi.nlm.nih.gov/24751541/)
- Kühlbrandt W**. 2014. Biochemistry. The resolution revolution. *Science* **343**:1443–1444. doi: [10.1126/science.1251652](https://doi.org/10.1126/science.1251652), PMID: [24675944](https://pubmed.ncbi.nlm.nih.gov/24675944/)
- Lawrence SL**, Feil SC, Morton CJ, Farrand AJ, Mulhern TD, Gorman MA, Wade KR, Tweten RK, Parker MW. 2015. Crystal structure of *Streptococcus pneumoniae* pneumolysin provides key insights into early steps of pore formation. *Scientific Reports* **5**:14352. doi: [10.1038/srep14352](https://doi.org/10.1038/srep14352), PMID: [26403197](https://pubmed.ncbi.nlm.nih.gov/26403197/)
- Letts JA**, Fiedorczuk K, Sazanov LA. 2016. The architecture of respiratory supercomplexes. *Nature* **537**:644–648. doi: [10.1038/nature19774](https://doi.org/10.1038/nature19774), PMID: [27654913](https://pubmed.ncbi.nlm.nih.gov/27654913/)

- Leung C**, Dudkina NV, Lukoyanova N, Hodel AW, Farabella I, Pandurangan AP, Jahan N, Pires Damaso M, Osmanović D, Reboul CF, Dunstone MA, Andrew PW, Lonnen R, Topf M, Saibil HR, Hoogenboom BW. 2014. Stepwise visualization of membrane pore formation by suliyisin, a bacterial cholesterol-dependent cytolysin. *eLife* **3**:e04247. doi: [10.7554/eLife.04247](https://doi.org/10.7554/eLife.04247), PMID: [25457051](https://pubmed.ncbi.nlm.nih.gov/25457051/)
- Li X**, Mooney P, Zheng S, Booth CR, Braunfeld MB, Gubbens S, Agard DA, Cheng Y. 2013. Electron counting and beam-induced motion correction enable near-atomic-resolution single-particle cryo-EM. *Nature Methods* **10**:584–590. doi: [10.1038/nmeth.2472](https://doi.org/10.1038/nmeth.2472), PMID: [23644547](https://pubmed.ncbi.nlm.nih.gov/23644547/)
- Liao M**, Cao E, Julius D, Cheng Y. 2013. Structure of the TRPV1 ion channel determined by electron cryo-microscopy. *Nature* **504**:107–112. doi: [10.1038/nature12822](https://doi.org/10.1038/nature12822), PMID: [24305160](https://pubmed.ncbi.nlm.nih.gov/24305160/)
- Lu P**, Bai XC, Ma D, Xie T, Yan C, Sun L, Yang G, Zhao Y, Zhou R, Scheres SH, Shi Y. 2014. Three-dimensional structure of human  $\gamma$ -secretase. *Nature* **512**:166–170. doi: [10.1038/nature13567](https://doi.org/10.1038/nature13567), PMID: [25043039](https://pubmed.ncbi.nlm.nih.gov/25043039/)
- Marshall JE**, Faraj BH, Gingras AR, Lonnen R, Sheikh MA, El-Mezgueldi M, Moody PC, Andrew PW, Wallis R. 2015. The crystal structure of pneumolysin at 2.0 Å resolution reveals the molecular packing of the pre-pore complex. *Scientific Reports* **5**:13293. doi: [10.1038/srep13293](https://doi.org/10.1038/srep13293), PMID: [26333773](https://pubmed.ncbi.nlm.nih.gov/26333773/)
- McCoy AJ**. 2007. Solving structures of protein complexes by molecular replacement with Phaser. *Acta Crystallographica Section D Biological Crystallography* **63**:32–41. doi: [10.1107/S0907444906045975](https://doi.org/10.1107/S0907444906045975), PMID: [17164524](https://pubmed.ncbi.nlm.nih.gov/17164524/)
- Mindell JA**, Grigorieff N. 2003. Accurate determination of local defocus and specimen tilt in electron microscopy. *Journal of Structural Biology* **142**:334–347. doi: [10.1016/S1047-8477\(03\)00069-8](https://doi.org/10.1016/S1047-8477(03)00069-8), PMID: [12781660](https://pubmed.ncbi.nlm.nih.gov/12781660/)
- Mulvihill E**, van Pee K, Mari SA, Müller DJ, Yildiz Ö. 2015. Directly observing the lipid-dependent self-assembly and pore-forming mechanism of the cytolytic toxin listeriolysin O. *Nano Letters* **15**:6965–6973. doi: [10.1021/acs.nanolett.5b02963](https://doi.org/10.1021/acs.nanolett.5b02963), PMID: [26302195](https://pubmed.ncbi.nlm.nih.gov/26302195/)
- Murshudov GN**, Vagin AA, Dodson EJ. 1997. Refinement of macromolecular structures by the maximum-likelihood method. *Acta Crystallographica Section D Biological Crystallography* **53**:240–255. doi: [10.1107/S0907444996012255](https://doi.org/10.1107/S0907444996012255), PMID: [15299926](https://pubmed.ncbi.nlm.nih.gov/15299926/)
- Nicastro D**, Schwartz C, Pierson J, Gaudette R, Porter ME, McIntosh JR. 2006. The molecular architecture of axonemes revealed by cryoelectron tomography. *Science* **313**:944–948. doi: [10.1126/science.1128618](https://doi.org/10.1126/science.1128618), PMID: [16917055](https://pubmed.ncbi.nlm.nih.gov/16917055/)
- Olofsson A**, Hebert H, Thelestam M. 1993. The projection structure of perfringolysin O (Clostridium perfringens theta-toxin). *FEBS Letters* **319**:125–127. doi: [10.1016/0014-5793\(93\)80050-5](https://doi.org/10.1016/0014-5793(93)80050-5), PMID: [8454043](https://pubmed.ncbi.nlm.nih.gov/8454043/)
- Pettersen EF**, Goddard TD, Huang CC, Couch GS, Greenblatt DM, Meng EC, Ferrin TE. 2004. UCSF chimera—a visualization system for exploratory research and analysis. *Journal of Computational Chemistry* **25**:1605–1612. doi: [10.1002/jcc.20084](https://doi.org/10.1002/jcc.20084), PMID: [15264254](https://pubmed.ncbi.nlm.nih.gov/15264254/)
- Ramachandran R**, Heuck AP, Tweten RK, Johnson AE. 2002. Structural insights into the membrane-anchoring mechanism of a cholesterol-dependent cytolysin. *Nature Structural Biology* **9**:823–827. doi: [10.1038/nsb855](https://doi.org/10.1038/nsb855), PMID: [12368903](https://pubmed.ncbi.nlm.nih.gov/12368903/)
- Ramachandran R**, Tweten RK, Johnson AE. 2005. The domains of a cholesterol-dependent cytolysin undergo a major FRET-detected rearrangement during pore formation. *PNAS* **102**:7139–7144. doi: [10.1073/pnas.0500556102](https://doi.org/10.1073/pnas.0500556102), PMID: [15878993](https://pubmed.ncbi.nlm.nih.gov/15878993/)
- Sato TK**, Tweten RK, Johnson AE. 2013. Disulfide-bond scanning reveals assembly state and  $\beta$ -strand tilt angle of the PFO  $\beta$ -barrel. *Nature Chemical Biology* **9**:383–389. doi: [10.1038/nchembio.1228](https://doi.org/10.1038/nchembio.1228), PMID: [23563525](https://pubmed.ncbi.nlm.nih.gov/23563525/)
- Scheres SH**. 2012. RELION: implementation of a bayesian approach to cryo-EM structure determination. *Journal of Structural Biology* **180**:519–530. doi: [10.1016/j.jsb.2012.09.006](https://doi.org/10.1016/j.jsb.2012.09.006), PMID: [23000701](https://pubmed.ncbi.nlm.nih.gov/23000701/)
- Scheres SH**. 2015. Semi-automated selection of cryo-EM particles in RELION-1.3. *Journal of Structural Biology* **189**:114–122. doi: [10.1016/j.jsb.2014.11.010](https://doi.org/10.1016/j.jsb.2014.11.010), PMID: [25486611](https://pubmed.ncbi.nlm.nih.gov/25486611/)
- Schrödinger LLC**. 2015. The PyMOL Molecular Graphics System. *PyMol*. Version 1.8.
- Shatursky O**, Heuck AP, Shepard LA, Rossjohn J, Parker MW, Johnson AE, Tweten RK. 1999. The mechanism of membrane insertion for a cholesterol-dependent cytolysin: a novel paradigm for pore-forming toxins. *Cell* **99**:293–299. doi: [10.1016/s0092-8674\(00\)81660-8](https://doi.org/10.1016/s0092-8674(00)81660-8), PMID: [10555145](https://pubmed.ncbi.nlm.nih.gov/10555145/)
- Shepard LA**, Heuck AP, Hamman BD, Rossjohn J, Parker MW, Ryan KR, Johnson AE, Tweten RK. 1998. Identification of a membrane-spanning domain of the thiol-activated pore-forming toxin clostridium perfringens perfringolysin O: an alpha-helical to beta-sheet transition identified by fluorescence spectroscopy. *Biochemistry* **37**:14563–14574. doi: [10.1021/bi981452f](https://doi.org/10.1021/bi981452f), PMID: [9772185](https://pubmed.ncbi.nlm.nih.gov/9772185/)
- Soltani CE**, Hotze EM, Johnson AE, Tweten RK. 2007a. Specific protein-membrane contacts are required for prepore and pore assembly by a cholesterol-dependent cytolysin. *Journal of Biological Chemistry* **282**:15709–15716. doi: [10.1074/jbc.M701173200](https://doi.org/10.1074/jbc.M701173200), PMID: [17412689](https://pubmed.ncbi.nlm.nih.gov/17412689/)
- Soltani CE**, Hotze EM, Johnson AE, Tweten RK. 2007b. Structural elements of the cholesterol-dependent cytolysins that are responsible for their cholesterol-sensitive membrane interactions. *PNAS* **104**:20226–20231. doi: [10.1073/pnas.0708104105](https://doi.org/10.1073/pnas.0708104105), PMID: [18077338](https://pubmed.ncbi.nlm.nih.gov/18077338/)
- Tang G**, Peng L, Baldwin PR, Mann DS, Jiang W, Rees I, Ludtke SJ. 2007. EMAN2: an extensible image processing suite for electron microscopy. *Journal of Structural Biology* **157**:38–46. doi: [10.1016/j.jsb.2006.05.009](https://doi.org/10.1016/j.jsb.2006.05.009), PMID: [16859925](https://pubmed.ncbi.nlm.nih.gov/16859925/)
- Terwilliger T**. 2004. SOLVE and RESOLVE: automated structure solution, density modification and model building. *Journal of Synchrotron Radiation* **11**:49–52. doi: [10.1107/S0909049503023938](https://doi.org/10.1107/S0909049503023938), PMID: [14646132](https://pubmed.ncbi.nlm.nih.gov/14646132/)
- Tilley SJ**, Orlova EV, Gilbert RJ, Andrew PW, Saibil HR. 2005. Structural basis of pore formation by the bacterial toxin pneumolysin. *Cell* **121**:247–256. doi: [10.1016/j.cell.2005.02.033](https://doi.org/10.1016/j.cell.2005.02.033), PMID: [15851031](https://pubmed.ncbi.nlm.nih.gov/15851031/)

- Tweten RK**, Parker MW, Johnson AE. 2001. The cholesterol-dependent cytolysins. *Current Topics in Microbiology and Immunology* **257**:15–33. doi: [10.1007/978-3-642-56508-3\\_2](https://doi.org/10.1007/978-3-642-56508-3_2), PMID: [11417120](https://pubmed.ncbi.nlm.nih.gov/11417120/)
- Tweten RK**. 2005. Cholesterol-dependent cytolysins, a family of versatile pore-forming toxins. *Infection and Immunity* **73**:6199–6209. doi: [10.1128/IAI.73.10.6199-6209.2005](https://doi.org/10.1128/IAI.73.10.6199-6209.2005), PMID: [16177291](https://pubmed.ncbi.nlm.nih.gov/16177291/)
- van Pee K**, Mulvihill E, Müller DJ, Yildiz Ö. 2016. Unraveling the pore-forming steps of pneumolysin from *Streptococcus pneumoniae*. *Nano Letters* **16**:7915–7924. doi: [10.1021/acs.nanolett.6b04219](https://doi.org/10.1021/acs.nanolett.6b04219), PMID: [27796097](https://pubmed.ncbi.nlm.nih.gov/27796097/)
- Weis S**, Palmer M. 2001. Streptolysin O: the C-terminal, tryptophan-rich domain carries functional sites for both membrane binding and self-interaction but not for stable oligomerization. *Biochimica Et Biophysica Acta (BBA) - Biomembranes* **1510**:292–299. doi: [10.1016/S0005-2736\(00\)00360-6](https://doi.org/10.1016/S0005-2736(00)00360-6), PMID: [11342166](https://pubmed.ncbi.nlm.nih.gov/11342166/)
- Zwart PH**, Afonine PV, Grosse-Kunstleve RW, Hung LW, Ioerger TR, McCoy AJ, McKee E, Moriarty NW, Read RJ, Sacchettini JC, Sauter NK, Storoni LC, Terwilliger TC, Adams PD. 2008. Automated structure solution with the PHENIX suite. *Methods in Molecular Biology* **426**:419–435. doi: [10.1007/978-1-60327-058-8\\_28](https://doi.org/10.1007/978-1-60327-058-8_28), PMID: [18542881](https://pubmed.ncbi.nlm.nih.gov/18542881/)